

Analytic Image Reconstruction Methods

PAUL E. KINAHAN*, MICHEL DEFRISÉ†, and ROLF CLACKDOYLE‡

*Department of Radiology, University of Washington, Seattle, Washington

†Division of Nuclear Medicine, Vrije Universiteit Brussel, Brussels, Belgium

‡Department of Radiology, University of Utah, Salt Lake City, Utah

- I. Introduction
- II. Data Acquisition
- III. The Central Section Theorem
- IV. Two-Dimensional Image Reconstruction
- V. Three-Dimensional Image Reconstruction from X-Ray Projections
- VI. Summary

I. INTRODUCTION

The purpose of tomographic image reconstruction is to start with the data acquired by the scanner and arrive at a true cross-sectional image. (*Tomo* comes from the Greek for “slice.”) In nuclear medicine with positron emission tomography (PET) and single-photon emission computed tomography (SPECT) we are typically forming images of a patient’s *in vivo* radiolabeled tracer distribution to obtain functional information. The same principles of image reconstruction, however, apply to anatomic imaging, particularly X-ray computed tomographic imaging, and also to nonmedical imaging modalities as diverse as radioastronomy and electron microscopy.

This chapter has two purposes: to review the theory of standard two-dimensional and three-dimensional analytic image reconstruction methods and to summarize theoretical developments in three-dimensional reconstruction methods. We start by formulating a mathematical model of the acquisi-

tion process that allows us to propose solutions to the inverse problem. These solutions give some insight into tomography in general and also the key difference between two- and three-dimensional imaging—that of data redundancy.

There are several excellent general references on image reconstruction with a broader scope than nuclear medicine, both at the introductory (Herman, 1980; Kak and Slaney, 1988; Natterer and Wübbeling, 2001) and advanced levels (Varrett and Swindell, 1981; Deans, 1983; Natterer, 1986). For completeness we mention here some image reconstruction topics that are *not* covered in this chapter.

- Iterative methods are an important class of reconstruction algorithms, especially in cases in which more accurate modeling of the acquisition process is important. This topic is discussed in Lalush and Wernick (Chapter 21 in this volume) and the reader is also referred to the review articles by Ollinger and Fessler (1997) and Leahy and Qi (2000).
- Reconstruction methods for data collected from scanners that acquire complex divergent projections, such as cone-beam SPECT and multirow helical computed tomography (CT), is a rapidly evolving field. For more information on these approaches the reader is referred to the proceedings of the biannual International Meeting on Fully Three-Dimensional Image Reconstruction in Nuclear Medicine and Radiology (“1991 International Meeting,” 1992; “1993 International Meeting,” 1994; “1995 International Meeting,” 1996; “1997 International Meeting,” 1998; “1999 International Meeting,” 2001; “2001 International Meeting,” 2002) commonly known as the “3D Meetings.”

- Efficient algorithms have been developed for various operators used in the reconstruction process, such as forward projection, backprojection, and filtering. Descriptions of these methods are scattered throughout the literature, with many in the following journals: *IEEE Transactions on Medical Imaging*, *IEEE Transactions on Nuclear Science*, *Physics in Medicine and Biology*, and *Medical Physics*.
- All functional imaging methods are necessarily dynamic at some level; however, in this chapter we assume a static tracer distribution to simplify our model. Four-dimensional (4D) reconstruction methods that incorporate the time-varying tracer distribution have also been developed (see Lalush and Wernick, Chapter 21 in this volume), as have retrospective kinetic modeling approaches to analyzing dynamic image sequences (see Morris, *et al.*, Chapter 23 in this volume).

The structure of this chapter is as follows. In Section II we describe a simple model of the data acquisition process. We then show in Section III how the Fourier transforms of the data and the original object are related through the central section theorem, also known as the central slice theorem. The central section theorem is used to explain two-dimensional image reconstruction in Section IV and three-dimensional image reconstruction in Section V. Section V also contains a presentation of the new theoretical results alluded to at the beginning of this introduction. Although the motivation of this work is the reconstruction of nuclear medicine images, the theoretical results can be applied to any modality that acquires line-integral data.

II. DATA ACQUISITION

The physics of photon generation and detection for the different imaging modalities are described elsewhere in this book. We use PET imaging here to motivate a line-integral model of the acquisition. The data acquisition processes for SPECT and X-ray CT can be related to the same model, as described, for example, by Shung *et al.* (1992).

We start by considering the parallelepiped joining any two detector elements as a volume of response (VOR) (Figure 1). In the absence of physical effects such as attenuation, scattered and accidental coincidences, and detector efficiency variations, the total number of coincidence events detected will be proportional to the total amount of tracer contained in the hypothetical tube or VOR, as indicated by the shaded area in Figure 1b. Because photon counting from radioactive decay is a random process, we have:

$$E\{\text{photons detected per second}\} = \iiint_{\text{VOR}} s(\mathbf{x})f(\mathbf{x})d\mathbf{x} \quad (1)$$

where $E\{\}$ is the expectation operator, $s(\mathbf{x})$ is the sensitivity within the tube at $\mathbf{x} = (x, y, z)$, and $f(\mathbf{x})$ is the three-

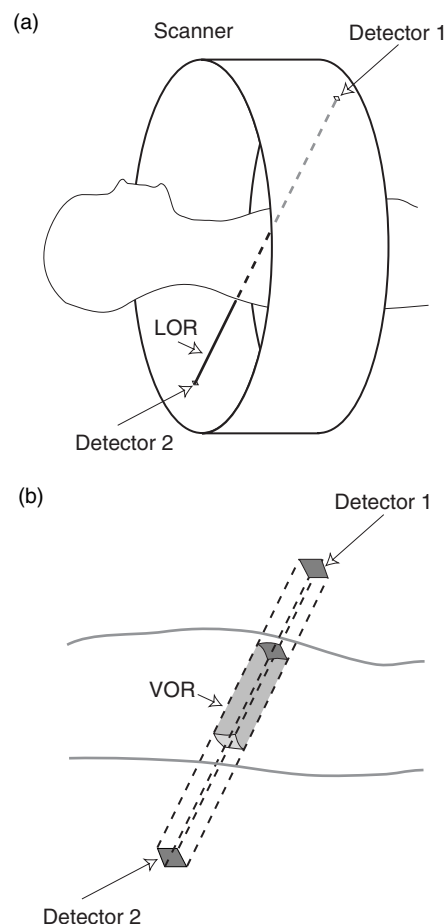


FIGURE 1 Tube, or volume of response, (VOR) corresponding to sensitive region scanned by two detector elements. (a) Overall scheme with the volume indicated as a line of response (LOR). (b) Detail showing VOR scanned by two of the rectangular detector elements (not to scale).

dimensional distribution of radiotracer activity inside the patient. With Eq. (1) we can make a more accurate statement of our inverse problem: Given a set of noisy measurements for all volumes of response, what is the original $f(\mathbf{x})$? The process of estimating $f(\mathbf{x})$ from the measured data is called image reconstruction.

To develop a theoretical basis for analytic image reconstruction from line-integral data we require several assumptions about the scanning process, including continuous sampling and the absence of physical effects such as attenuation, scatter, radiotracer half-life, and collimator blurring. We assume the cross-sectional area of the parallelepiped tube becomes zero so that we are integrating along a line. In other words, the sensitivity $s(\mathbf{x})$ becomes a delta function, which is nonzero only along a specified line of response (LOR). We also assume that there is no statistical noise, which allows us to develop exact solutions. As discussed later, the presence of statistical noise means that no exact

solution exists, so in practice some form of regularization is required. In addition, we only consider real-world functions $f(\mathbf{x})$ (compactly supported and square-integrable) that are nonpathological in any mathematical sense (Natterer, 1986).

All the simplifying assumptions are violated in practice. It is possible, however, to accurately model the physics of the acquisition, as described by Leahy and Qi (2000). These models typically lead to large sets of equations that can only be inverted with iterative techniques. Based on our line-integral model, however, we are able to derive theoretical insights that lead to image reconstruction algorithms that are useful in practice.

A. Two-Dimensional Imaging

For two-dimensional imaging we only consider LORs lying within a specified imaging plane. The acquired data are collected along a LOR through a two-dimensional object $f(x,y)$ as indicated in Figure 2, and we write Eq. (1) as a line integral. In two dimensions, we can express the line integral acquisition model by use of a rotated coordinate system, with a counter-clockwise rotation of ϕ (Figure 2). The rotated coordinates (subscript r) are related to the original coordinates by:

$$\begin{bmatrix} x \\ y \end{bmatrix} = \begin{bmatrix} \cos \phi & -\sin \phi \\ \sin \phi & \cos \phi \end{bmatrix} \begin{bmatrix} x_r \\ y_r \end{bmatrix} \quad (2)$$

With this notation we can compactly rewrite Eq. (1) as:

$$p(x_r, \phi) = \int_{-\infty}^{\infty} f(x, y) dy_r \quad (3)$$

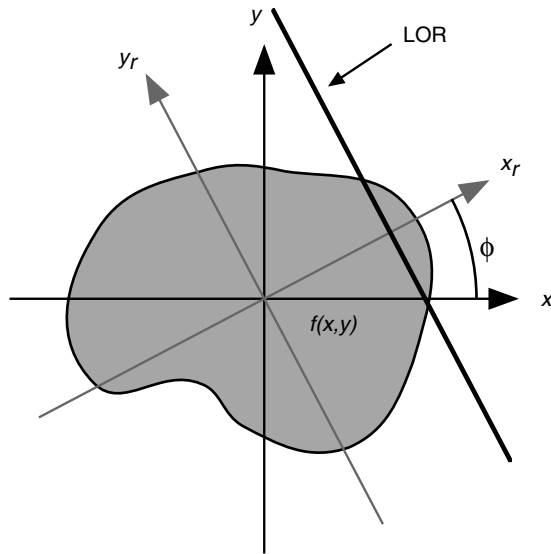


FIGURE 2 Two-dimensional LOR example. The value of $f(x,y)$ is integrated along the LOR to obtain $p(x_r, \phi)$.

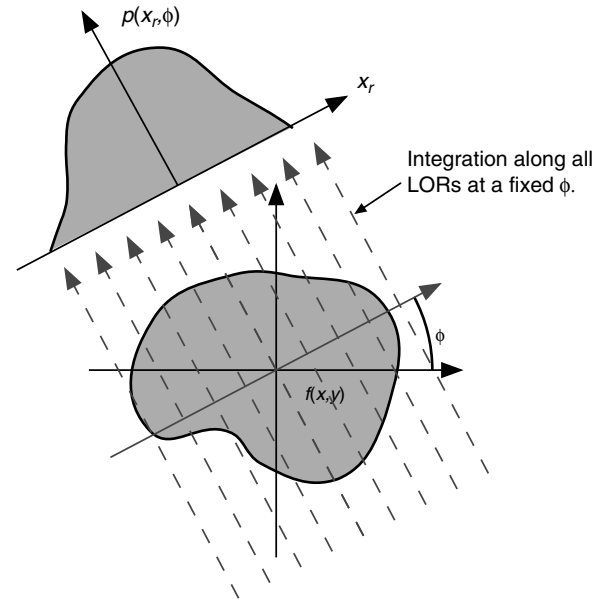


FIGURE 3 A projection formed from integration along all parallel LORs at an angle ϕ .

where the location of the LOR is described by x_r and ϕ , and $p(x_r, \phi)$ is the integral of $f(x,y)$ along the LOR. The image reconstruction problem can now be explicitly defined. Given $p(x_r, \phi)$ for all x_r and ϕ , what is the original function $f(x,y)$? In the presence of statistical noise, no exact solution is possible. Approaches constraining the solution by regularization methods are discussed after we have arrived at an exact solution for noiseless data.

For a fixed direction, ϕ , the set of line-integral data for all x_r forms a projection of $f(x,y)$ as shown in Figure 3. The collection of all projections for $0 \leq \phi < 2\pi$ as a two-dimensional function of x_r and ϕ has been termed a *sino-gram* by the Swedish scientist Paul Edholm because the set of LORs passing through a fixed point (x_0, y_0) lie along a sinusoid described by $x_r = x_0 \cos \phi + y_0 \sin \phi$. This relationship is illustrated in Figure 4. A sinogram for a general object will be the linear superposition of all sinusoids corresponding to each point in the object.

At this point we make several comments about sinograms and projections:

1. The line-integral transform of $f(x,y) \rightarrow p(x_r, \phi)$ is called the *X-ray transform* (Natterer and Wübbeling, 2001), which in 2D is the same as the *Radon transform* as we describe later. The X-ray transform (or variants thereof) is a basis for a model of the data acquisition process of several modalities, including gamma cameras, SPECT, PET, and X-ray imaging systems, as well as several nonmedical imaging modalities.
2. Line-integral projections are periodic ($p(x_r, \phi + 2\pi) = p(x_r, \phi)$) and have an odd symmetry in the sense that $p(x_r, \phi) = -p(-x_r, \phi + \pi)$. If this symmetry condition holds with measured data, then the angular range of sinograms

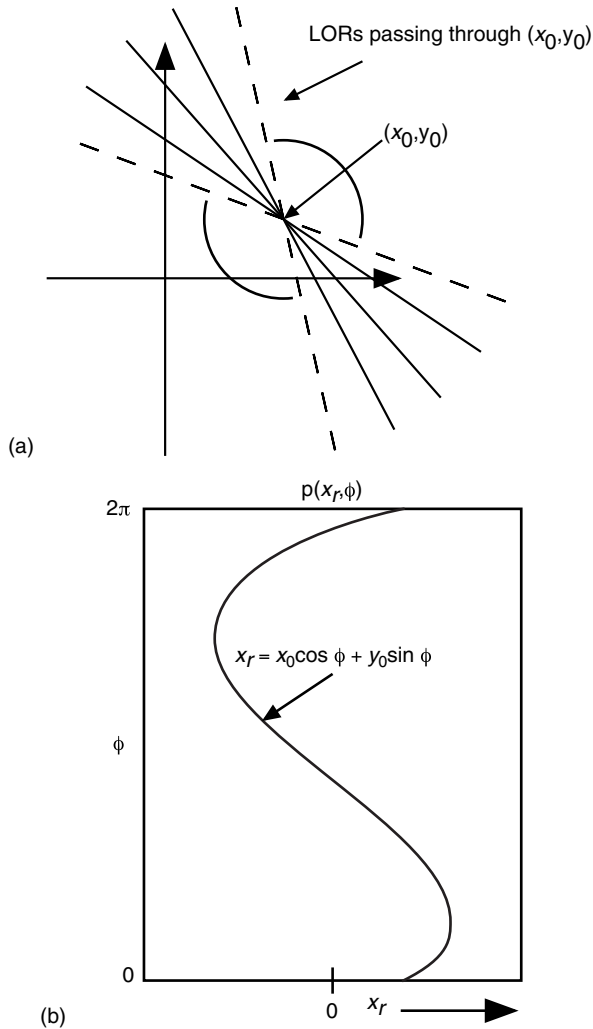


FIGURE 4 (a) Relation between LORs passing through a fixed point (x_0, y_0) and (b) the loci of integrated $p(x_r, \phi)$ values in the sinogram.

can, in principle, be constrained to $0 \leq \phi < \pi$. In many cases, such as SPECT imaging, in which the collimators introduce a depth-dependent response, we have $p(x_r, \phi) \neq p(-x_r, \phi + \pi)$, and so the full range $0 \leq \phi < 2\pi$ must be used.

3. The X-ray transform $f(x, y) \rightarrow p(x_r, \phi)$ is performed by the imaging process itself (that is, the scanner) and may at first glance appear to be a mapping from rectangular to polar coordinates. This is not the case, as is seen by considering that $p(0, \phi_1) \neq p(0, \phi_2)$ for $\phi_1 \neq \phi_2$. With the aid of the central section theorem, however, we will see that there is a mapping from rectangular to polar coordinates in the Fourier domain.
4. The integral of Eq. (3) is over the infinite real line, but as the tracer concentration in the patient is contained in the scanner field of view (FOV), with radius R_{FOV} , we have $f(x, y) \equiv 0$ for $x^2 + y^2 \geq R_{\text{FOV}}^2$, so the only contribution to the integral occurs for $-R_{\text{FOV}} < x_r < R_{\text{FOV}}$.

5. We have discussed data acquisition of a two-dimensional function, although any tracer distribution is three-dimensional. A more accurate statement would be to say that we have imaged one transverse plane at $z = z_0$, for which we can reexpress Eq. (3) as,

$$p(x_r, \phi, z = z_0) = \int_{-\infty}^{\infty} f(x, y, z = z_0) dy, \quad (4)$$

We can thus image a volumetric object by repeating the acquisition for a desired range of z . If the sinogram for each value of z is reconstructed, we can stack the image planes together to form a three-dimensional image of $f(x, y, z)$. Although this can be considered a form of three-dimensional imaging, it is different from the fully three-dimensional acquisition model described in the next section.

B. Fully Three-Dimensional Imaging

In fully three-dimensional imaging we include both the two-dimensional line-integral data for all imaging planes perpendicular to the scanner or patient axis, called *direct planes*, as well as the line-integral data lying on oblique imaging planes that cross the direct planes, as shown in Figure 5. This type of data is typically collected by PET scanners to increase sensitivity and lower the statistical noise associated with photon counting, thus improving the signal-to-noise ratio (SNR) in the reconstructed image.

For the X-ray transform of a three-dimensional object, four parameters are needed to parameterize the LOR shown in Figure 5: two angles (ϕ, θ) to define the unit vector $\hat{z}_r(\phi, \theta) = (\cos \phi \cos \theta, \sin \phi \cos \theta, \sin \theta)$ parallel to the LOR,

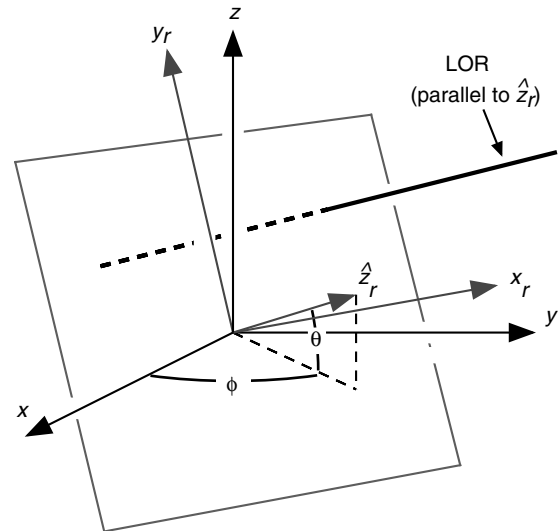


FIGURE 5 Parameterization of a three-dimensional LOR for the X-ray transform using a rotated coordinate frame. Note that the scanner axis, z , is vertical (for mathematical convention) rather than the implied horizontal direction in Figure 1.

and two coordinates (x_r, y_r) to locate the intersection of the LOR with the plane perpendicular to $\hat{z}_r(\phi, \theta)$.

By using the constraint $\hat{x}_r \cdot \hat{z} = 0$ and the definition of θ as the co-polar angle, the rotated coordinates are related to the original coordinates by:

$$\begin{bmatrix} x \\ y \\ z \end{bmatrix} = \begin{bmatrix} -\sin \phi & -\cos \phi \sin \theta & \cos \phi \cos \theta \\ \cos \phi & -\sin \phi \sin \theta & \sin \phi \cos \theta \\ 0 & \cos \theta & \sin \theta \end{bmatrix} \begin{bmatrix} x_r \\ y_r \\ z_r \end{bmatrix} \quad (5)$$

This choice of rotated coordinates and θ as the co-polar angle is customary because the equivalent two-dimensional data acquisition, or the direct planes, corresponds to $\theta = 0$. In addition, the (x_r, y_r) coordinates are in an appropriate orientation for viewing individual two-dimensional projections for a fixed $\hat{z}_r(\phi, \theta)$. Using the coordinate transform of Eq. (5), the line-integral projections along the LOR, located by (x_r, y_r, ϕ, θ) , are easily expressed as:

$$p(x_r, y_r, \phi, \theta) = \int_{-\infty}^{\infty} f(x, y, z) dz_r \quad (6)$$

For a fixed direction, $\hat{z}_r(\phi, \theta)$, the set of line-integral data for all (x_r, y_r) forms a two-dimensional projection $p(x_r, y_r, \phi, \theta)$ of $f(x, y, z)$ as illustrated in Figure 6.

It is often convenient to regard $p(x_r, y_r, \phi, \theta)$ as a two-dimensional projection in the direction $\hat{z}_r(\phi, \theta)$. The full projection data set, however, is a four-dimensional function, so the X-ray transform of $f(x, y, z) \rightarrow p(x_r, y_r, \phi, \theta)$ has increased the number of dimensions by one, and we show later that this causes redundancies in the data.

The projection data set $p(x_r, y_r, \phi, \theta)$ is defined for $|x_r, y_r| < \infty$, $0 \leq \phi < \pi$, and $|\theta| < \pi/2$ because there are similar symmetries as for the two-dimensional case:

$$\begin{aligned} p(x_r, y_r, \phi, \theta) &= p(x_r, y_r, \phi + 2\pi, \theta) \\ &= p(x_r, y_r, \phi, \theta + 2\pi) \\ &= p(-x_r, y_r, \phi + \pi, -\theta) \end{aligned} \quad (7)$$

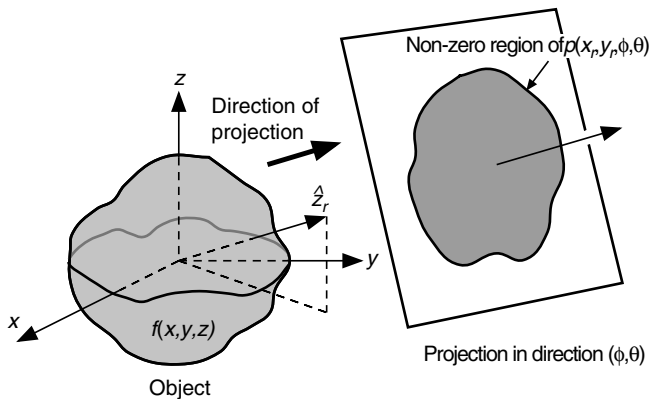


FIGURE 6 Illustration of a two-dimensional line-integral projection $p(x_r, y_r, \phi, \theta)$ of a three-dimensional object $f(x, y, z)$. The projection is formed from the set of all LORs parallel to $\hat{z}_r(\phi, \theta)$.

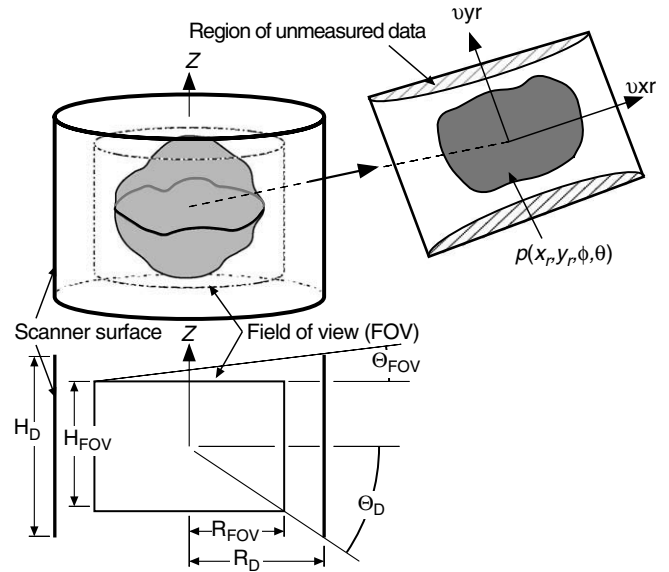


FIGURE 7 Range of measured data for $p(x_r, y_r, \phi, \theta)$ with the scanner detectors modeled as the curved wall of a cylindrical surface.

The range of nonzero values, however, is finite in x_r and y_r as indicated by Figure 7, with $|x_r| < R_{FOV}$ and $|y_r| < y_{r,lim}$, where $y_{r,lim} = y_{r,lim}(x_r, \theta; R_{FOV}, H_{FOV})$. We also note that although the maximum value of θ for which LORs are detected is $\Theta_D = \arctan(H_D/2R_D)$, the projections will have regions of unmeasured data for $\Theta_{FOV} < |\theta| \leq \Theta_D$, due to the finite axial extent of the scanner, where the limiting FOV angle, Θ_{FOV} , depends on the height and radius of the detector surface (H_D, R_D) and the FOV (H_{FOV}, R_{FOV}). The Fourier transform cannot be used with such truncated projections, which complicates the reconstruction process. In other words, the scanner response is no longer shift-invariant because the apparent intensity of a point source will depend on its location inside the field of view. To simplify our discussion, unless otherwise noted, we will assume that $|\theta| \leq \Theta_{FOV}$.

Finally, we note that the special case of $p(x_r, y_r, \phi, \theta = 0)$ is equivalent to an axial stack (Eq. (4)) of two-dimensional sinograms with $p(x_r, \phi, z = y_r) = p(x_r, y_r, \phi, \theta = 0)$. In other words, the data for $p(x_r, y_r, \phi, \theta = 0)$ provide sufficient information to reconstruct a volumetric image of the tracer distribution. The purpose of including the data for $p(x_r, y_r, \phi, \theta \neq 0)$ is to increase the number of detected photons used in estimating the tracer distribution, which will lower the statistical noise and improve the image SNR.

C. The Relationship between the Radon and X-Ray Transforms

In fully three-dimensional imaging it is possible to collect another type of projection in which we integrate $f(x, y, z)$ across all two-dimensional planes. This is called the *Radon transform* and is illustrated in Figure 8, which also shows

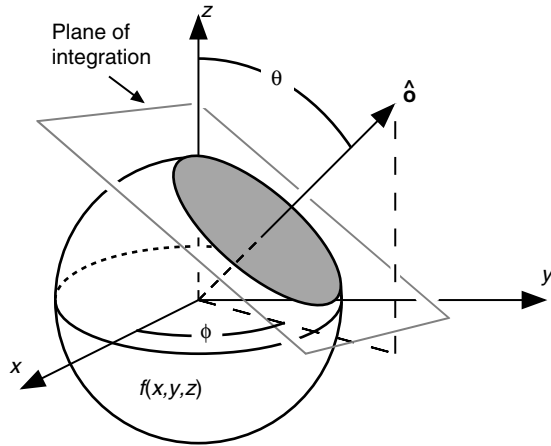


FIGURE 8 Illustration of a two-dimensional plane integral used for the Radon transform of a three-dimensional object. Note that in this case θ is used for the polar angle.

that nonzero values occur for only those planes that intersect the object.

For an n -dimensional object $f(\mathbf{x})$, $\mathbf{x} = (x_1, x_2, \dots, x_n)$, the Radon transform of $f(\mathbf{x})$ is defined as the set of all integrals along the $(k = n - 1)$ -dimensional hyperplanes intersecting the object. For our example, $n = 3$, so $k = 2$ and the Radon transform of a three-dimensional object is thus the set of integrals along all two-dimensional planes that intersect the object.

Using the same notation, the X-ray transform of an n -dimensional object is defined as the set of all $(k = 1)$ -dimensional line-integrals through the object. For our three-dimensional example (Figure 5), the X-ray transform is the set of all line-integrals through the object.

A convenient representation for the location of the plane is based on the vector $t\hat{\mathbf{o}}(\phi, \theta)$, where $t \in \mathbb{R}$ is the signed distance between the origin and the plane normal to $\hat{\mathbf{o}}(\phi, \theta) \in S^2$, where S^2 denotes the three-dimensional unit sphere. The formal expression for the Radon transform is compactly expressed by:

$$f(t, \hat{\mathbf{o}}) = f(t, \phi, \theta) = \iiint_{\mathbb{R}^3} f(\mathbf{x}) \delta(\mathbf{x} \cdot \hat{\mathbf{o}}(\phi, \theta) - t) d\mathbf{x} \quad (8)$$

where $\mathbf{x} = (x, y, z)$ and the Dirac delta function $\delta(x)$ has the sifting property $\int_a^c g(x) \delta(x - b) dx = g(b)$ if $a < b < c$. Here we use the nonitalicized $f(t, \phi, \theta)$ to represent the Radon transform of $f(x, y, z)$.

Because each planar integral is indexed by two angular variables (ϕ, θ) and one linear variable t , the Radon transform performs a mapping of a three-dimensional function $f(x, y, z)$ to a three-dimensional function $f(t, \phi, \theta)$ similar to the three-dimensional Fourier transform. In other words, each object is determined by its Radon transform and vice versa (in the absence of statistical noise)¹. This relationship

¹More precisely, the relationship is a unitary mapping between the derivative of the Radon transform and the object.

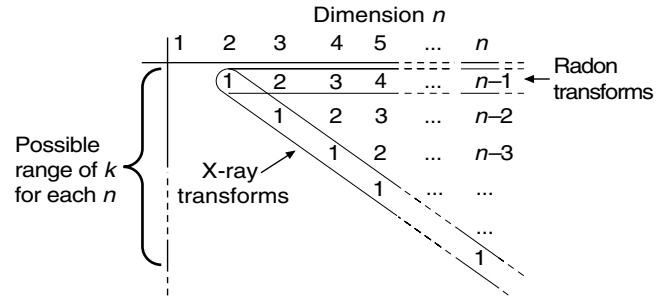


FIGURE 9 Schematic of the k -dimensional projection transforms for an n -dimensional object, where k ranges from $k = 1$ (the X-ray transform) to $k = n - 1$ (the Radon transform). For two-dimensional objects, the X-ray and Radon transforms are equivalent.

holds for any n -dimensional Radon transform, as discussed next.

For two-dimensional objects, the Radon and X-ray transform definitions coincide, as $k = n - 1 = 1$ (that is, line-integrals) for both, whereas for three- (or higher-) dimensional objects the X-ray transform remains a line-integral transform while the Radon transform becomes a plane integral for $n = 3$, and a hyperplane for $n > 3$. This family of k -dimensional projections for n -dimensional objects is illustrated in Figure 9, which also indicates the presence of other types of projections for $n \geq 4$. In nuclear medicine imaging the cases of most interest are, of course, $n = 2$ and $n = 3$, although the $n = 4$, $k = 2$ type of projection has found use in the *planogram* backprojection method (Brasse *et al.*, 2000).

For the $n = 3$ case, the $k = 1$ (X-ray transform) projections map $f(\mathbf{x})$, $\mathbf{x} \in \mathbb{R}^3$ to $p(x_r, y_r, \phi, \theta)$, $(x_r, y_r) \in \mathbb{R}^2$, and $(\phi, \theta) \in S^2$, where S^n is the unit sphere. For the $n = 3$ case, the $k = 2$ (Radon transform) projections map $f(\mathbf{x})$, $\mathbf{x} \in \mathbb{R}^3$ to $f(t, \phi, \theta)$, $t \in \mathbb{R}^1$, and $(\phi, \theta) \in S^2$. In other words, $f(\mathbf{x})$ is defined on \mathbb{R}^3 , $p(x_r, y_r, \phi, \theta)$ is defined on $\mathbb{R}^2 \times S^2$, and $f(t, \phi, \theta)$ is defined on $\mathbb{R}^1 \times S^2$. In general, the k -dimensional projection transforms for an n -dimensional object are defined on $\mathbb{R}^{n-k} \times S^{n-1}$. We note that unlike the $n = 2$ case, the increase in dimensionality for the $n = 3$ X-ray transform implies redundancy in $p(x_r, y_r, \phi, \theta)$. The Radon transform $f(t, \phi, \theta)$, however, still has the same number of dimensions as $f(\mathbf{x})$. This is true for the Radon transform in any dimension, actually, because the n -dimensional Radon transform ($k = n - 1$) is defined on $\mathbb{R}^1 \times S^{n-1}$. The general theory of k -dimensional projections is discussed by Keinert (1989).

III. THE CENTRAL SECTION THEOREM

The central section theorem (also known as the central slice or projection slice theorem) is the most important relationship in analytic image reconstruction. In this section we first derive the two-dimensional version, which is then easily

extended to the three-dimensional X-ray transform. We then discuss the version for the three-dimensional Radon transform and generalizations for other transforms. For all the results presented here, we require that the imaging process be shift-invariant, which allows the use of Fourier transforms. By *shift-invariance* we mean that if we scan a shifted object, the projections are also shifted but are otherwise identical to the projections of the unshifted object. Shift-invariance is a natural property of two-dimensional imaging. For fully three-dimensional imaging situation is somewhat more complicated, but for now we assume the data are shift-invariant.

A. The Two-Dimensional Central Section Theorem

1. Derivation

We start by recalling the definition of the one-dimensional Fourier transform and the inverse transform:

$$\begin{aligned} F(v_x) &= F_1\{f(x)\} = \int_{-\infty}^{\infty} f(x) e^{-i2\pi v_x x} dx \\ f(x) &= F_1^{-1}\{F(v_x)\} = \int_{-\infty}^{\infty} F(v_x) e^{i2\pi v_x x} dv_x \end{aligned} \quad (9)$$

where we adopt the notation of capital letters for Fourier transformed functions, and, in general, the operator $F_n\{f(\mathbf{x})\}$ for the n -dimensional Fourier transform of $f(\mathbf{x})$, $F_n^{-1}\{F(\mathbf{u})\}$ for the inverse n -dimensional Fourier transform, and v_x as the Fourier space conjugate of x .

The one-dimensional Fourier transform of a projection is given by:

$$P(v_{xr}, \phi) = F_1\{p(x_r, \phi)\} = \int_{-\infty}^{\infty} p(x_r, \phi) e^{-i2\pi v_{xr} x_r} dx_r \quad (10)$$

An important step is the introduction of the definition of $p(x_r, \phi)$ from Eq. (3),

$$\begin{aligned} P(v_{xr}, \phi) &= \int_{-\infty}^{\infty} p(x_r, \phi) e^{-i2\pi v_{xr} x_r} dx_r \\ &= \int_{-\infty}^{\infty} \int_{-\infty}^{\infty} f(x, y) e^{-i2\pi v_{xr} x_r} dx_r dy_r \\ &= \int_{-\infty}^{\infty} \int_{-\infty}^{\infty} f(x, y) e^{-i2\pi (x \cos \phi + y \sin \phi) v_{xr}} dx dy \\ &= F(v_{xr} \cos \phi, v_{xr} \sin \phi) \end{aligned} \quad (11)$$

where $F(v_x, v_y) = F_2\{f(x, y)\} = \int_{-\infty}^{\infty} \int_{-\infty}^{\infty} f(x, y) e^{-i2\pi (x v_x + y v_y)} dx dy$. Because the Fourier transform is invariant under rotation, we have from Eq. (2):

$$\begin{bmatrix} v_x \\ v_y \end{bmatrix} = \begin{bmatrix} \cos \phi & -\sin \phi \\ \sin \phi & \cos \phi \end{bmatrix} \begin{bmatrix} v_{xr} \\ v_{yr} \end{bmatrix} \quad (12)$$

We can use Eq. (12) to more concisely express Eq. (11) as:

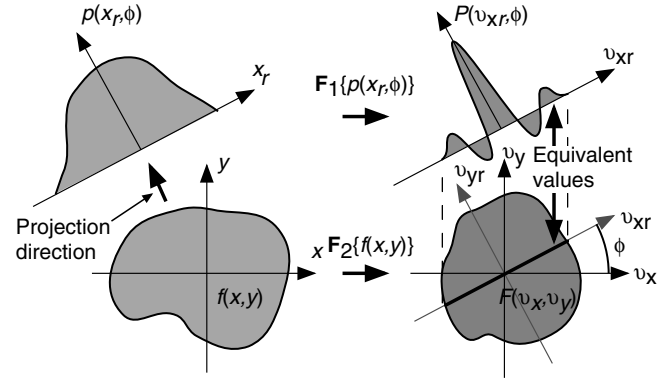


FIGURE 10 Two-dimensional central section theorem, showing the equivalency between the one-dimensional Fourier transform of a projection at angle ϕ and the central section at the same angle through the two-dimensional Fourier transform of the object.

$$P(v_{xr}, \phi) = F(v_x, v_y) \Big|_{v_y=0} \quad (13)$$

Equation (13) is a key to understanding tomographic imaging. It shows that the Fourier transform of a one-dimensional projection is equivalent to a section, or profile, at the same angle through the center of the two-dimensional Fourier transform of the object. This is illustrated in Figure 10.

2. Data Sufficiency

Because any function is uniquely determined by its Fourier transform (that is, it can be computed via the inverse Fourier transform), the central section theorem indicates that if we know $P(v_{xr}, \phi)$ at all angles $0 \leq \phi < \pi$, then we can somehow determine $F(v_x, v_y)$ and thus $f(x, y)$. This is the approach we take in the next section. We can also establish the conditions for necessary and sufficient data. To determine $F(v_x, v_y)$ and thus $f(x, y)$, we need $p(x_r, \phi)$ for $-R_{FOV} < x_r < R_{FOV}$ and $0 \leq \phi < \pi$.

B. The Three-Dimensional Central Section Theorem for X-Ray Projections

1. Derivation

For fully three-dimensional imaging the X-ray and Radon transforms have different versions of the central section theorem. For the Radon transform version the reader is referred to Deans (1983, chap. 4) and Section IIIC. A version of the central section theorem valid for all n and k (Figure 9) is given by Keinert (1989).

To derive the central section theorem for the X-ray projection of a three-dimensional object we first compute the two-dimensional Fourier transform with respect to the first two (linear) variables:

$$P(v_{xr}, v_{yr}, \phi, \theta) = \int_{-\infty}^{\infty} \int_{-\infty}^{\infty} p(x_r, y_r, \phi, \theta) e^{-i2\pi (x_r v_{xr} + y_r v_{yr})} dx_r dy_r \quad (14)$$

If $F(v_x, v_y, v_z)$ is the three-dimensional Fourier transform of $f(x, y, z)$,

$$F(v_x, v_y, v_z) = \int_{-\infty}^{\infty} \int_{-\infty}^{\infty} \int_{-\infty}^{\infty} f(x, y, z) e^{-i2\pi(xv_x + yv_y + zv_z)} dx dy dz \quad (15)$$

then by using a derivation similar to Eq. (15), we arrive at the three-dimensional version of the central section theorem for X-ray projections:

$$P(v_{xr}, v_{yr}, \phi, \theta) = F(v_x, v_y, v_z) \Big|_{v_z=0} \quad (16)$$

where from Eq. (5) we have,

$$\begin{bmatrix} v_x \\ v_y \\ v_z \end{bmatrix} = \begin{bmatrix} -\sin \phi & -\cos \phi \sin \theta & \cos \phi \cos \theta \\ \cos \phi & -\sin \phi \sin \theta & \sin \phi \cos \theta \\ 0 & \cos \theta & \sin \theta \end{bmatrix} \begin{bmatrix} v_{xr} \\ v_{yr} \\ v_{zr} \end{bmatrix} \quad (17)$$

The meaning of the three-dimensional central section theorem for the X-ray projections is analogous to the two-dimensional case: A two-dimensional Fourier transform of a projection perpendicular to $\hat{z}_r(\phi, \theta)$ is equivalent to a section at the same orientation though the three-dimensional Fourier transform of the object. This is illustrated in Figure 11.

2. Data Sufficiency

As we did in the two-dimensional case, we can use the three-dimensional central section theorem to determine the conditions for necessary and sufficient data. It will be helpful to use the notation introduced by Orlov (1976a, 1976b). The orientation of a (nontruncated) projection can be identified by the location of the tip of the perpendicular unit vector $\hat{z}_r(\phi, \theta)$ on the unit sphere, and a set of such points associated with a set of projection orientations is designated Ω . Two sets of interest, $\Omega_0 = \{\hat{z}_r(\phi, \theta) | 0 \leq \phi < \pi, \theta = 0\}$ and $\Omega_\Theta = \{\hat{z}_r(\phi, \theta) | 0 \leq \phi < \pi, |\theta| \leq \Theta\}$, which correspond to multiplane two-dimensional and fully three-dimensional acquisitions, are shown in Figure 12.

Orlov's data sufficiency theorem states that a fully three-dimensional data set is sufficient if there is no great circle

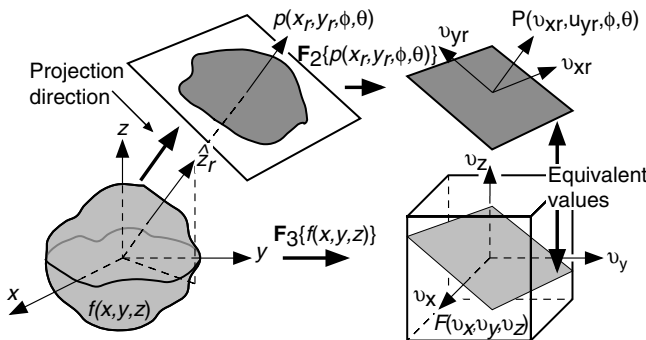


FIGURE 11 Three-dimensional central section theorem for X-ray transforms, showing the equivalency between the two-dimensional Fourier transform of a projection in direction $\hat{z}_r(\phi, \theta)$ and the central section at the same angle though the three-dimensional Fourier transform of the object.

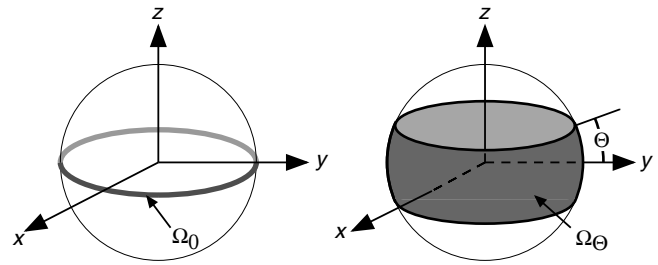


FIGURE 12 Sets of measured (and nontruncated) projections using Orlov's notation ($\Omega_0 = \{\hat{z}_r(\phi, \theta) | 0 \leq \phi < \pi, \theta = 0\}$ and $\Omega_\Theta = \{\hat{z}_r(\phi, \theta) | 0 \leq \phi < \pi, |\theta| \leq \Theta\}$) for two common cylindrical scanning geometries.

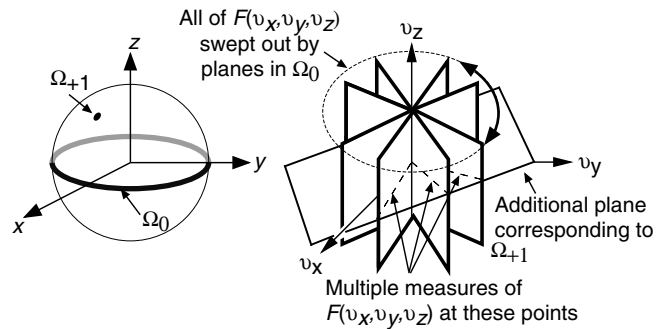


FIGURE 13 An example of data redundancy inherent in fully three-dimensional scanning even if only one additional projection Ω_{+1} is added to a two-dimensional data set (Ω_0).

on the unit sphere that does not intersect Ω (Orlov, 1976a). This is equivalent to saying that every part of the Fourier transform $F(v_x, v_y, v_z)$ is measured at least once.

The multiplane two-dimensional set Ω_0 is a subset of the fully three-dimensional set Ω_Θ , and because Ω_0 contains sufficient information to reconstruct $f(x, y, z)$ (because we know $P(v_{xr}, \phi)$ for each z), then Ω_Θ must contain redundant information. As a specific (albeit unusual) example, in Figure 13 the Fourier transforms of the set of projections corresponding to Ω_0 sweep out all of the volume of $F(v_x, v_y, v_z)$. A single additional projection, $\Omega_{+1} = \{\hat{z}_r(\phi_1, \theta_1) | \theta_1 \neq 0\}$, will contain redundant information along the corresponding oblique plane in Fourier space, and we can see that Ω_Θ contains a continuum of such redundant projections. As previously mentioned, we wish to use this redundant information to improve the image SNR.

3. Differences between Two-Dimensional and Fully Three-Dimensional Imaging

As a final comment, we note that we have seen two significant differences between two- and fully three-dimensional imaging: (1) the shift-variance of the scanner response when truncated projections are included, and (2) the redundancy of the fully three-dimensional data. Solutions for these issues are investigated after a review of two-dimensional image reconstruction.

C. Other Versions of the Central Section Theorem

So far we have only considered the $k = 1$ (X-ray transform) cases for $n = 2$ and $n = 3$. For the three-dimensional Radon transform, $f(t, \phi, \theta) = f(t, \hat{\mathbf{o}})$, we can compute the Fourier transform with respect to the linear variable $t \in \mathbb{R}^1$:

$$\begin{aligned} F(v, \phi, \theta) &= F_1[f(t, \phi, \theta)] \\ &= \int_{-\infty}^{\infty} \left[\iiint_{\mathbb{R}^3} f(\mathbf{x}) \delta(\mathbf{x} \cdot \hat{\mathbf{o}}(\phi, \theta) - t) d\mathbf{x} \right] e^{-i2\pi v t} dt \\ &= |v_t| \int_{-\infty}^{\infty} \left[\iiint_{\mathbb{R}^3} f(\mathbf{x}) e^{-i2\pi v_t t} \delta(\mathbf{x} \cdot v_t \hat{\mathbf{o}}(\phi, \theta) - v_t t) d\mathbf{x} \right] dt \end{aligned} \quad (18)$$

where we use the relationship $\delta(ax) = \delta(x)/|a|$. If we now define $v_t \hat{\mathbf{o}} = \mathbf{u} = (u_x, u_y, u_z)$ and $v_t t = \xi$, we have

$$\begin{aligned} F(v, \phi, \theta) &= \iiint_{\mathbb{R}^3} \left[\int_{-\infty}^{\infty} f(\mathbf{x}) e^{-i2\pi \xi} \delta(\mathbf{x} \cdot \mathbf{u} - \xi) d\xi \right] d\mathbf{x} \\ &= \iiint_{\mathbb{R}^3} f(\mathbf{x}) e^{-i2\pi \mathbf{x} \cdot \mathbf{u}} d\mathbf{x} \\ &= F(\mathbf{u}) \end{aligned} \quad (19)$$

so along the line in frequency space defined by $v_t \hat{\mathbf{o}} = \mathbf{u}$, we have

(20)

In words, Eq. (20) says that the one-dimensional Fourier transform along the line through the origin of the Radon transform, with direction $\hat{\mathbf{o}}$, is equivalent to values along the line $v_t \hat{\mathbf{o}}$ through the three-dimensional Fourier transform of the object. This is expressed in Figure 14 for the general n -dimensional Radon transform with added generalization of the direction vector to $\hat{\mathbf{o}} \in \mathbb{S}^{n-1}$, where \mathbb{S}^{n-1} is the unit

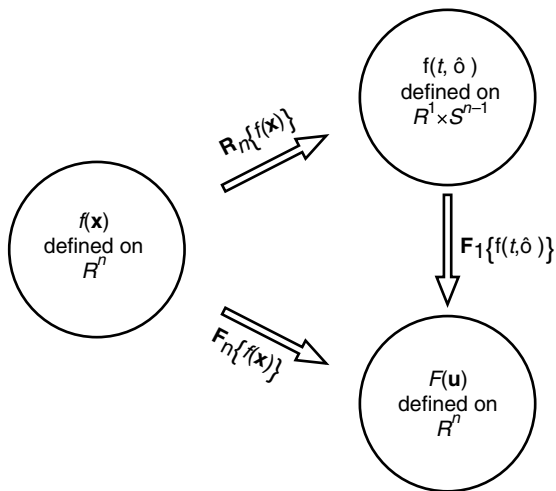


FIGURE 14 Outline of the central section theorem for the n -dimensional Radon transform. Note the correspondence to the central section theorem for X-ray transforms in Figures 10 and 11.

sphere in n -dimensions and in two-dimensions this reduces to Eq. (14). Finally, we note that appropriate versions of the central section theorem exist for all k -dimensional projections of an n -dimensional object (Figure 9) (Keinert, 1989).

IV. TWO-DIMENSIONAL IMAGE RECONSTRUCTION

A. Backprojection

An essential step in image reconstruction is backprojection, which is the adjoint to forward projection and is defined as:

$$b(x, y) = \int_0^\pi p(x_r, \phi) d\phi \quad (21)$$

where $x_r = x \cos \phi + y \sin \phi$ from the inverse of Eq. (2). Equation (21) implies that the appropriate value of $p(x_r, \phi)$ is summed over all ϕ for each image element (x, y) in turn. A more efficient procedure is illustrated in Figure 15, where for each value of ϕ all the image elements (x, y) are updated with the appropriate values of $p(x_r, \phi)$.

Conceptually this form of backprojection can be described as placing a value of $p(x_r, \phi)$ back into an image array along the appropriate LOR, but because the knowledge of where the values came from was lost in the integration with respect to y_r (see Eq. 3) the best we can do is place a constant value into elements along the LOR. This can be described as:

$$b^1(x, y; \phi) = p(x_r, \phi) \quad (22)$$

where $b^1(x, y; \phi)$ signifies the two-dimensional function formed by backprojecting the single projection indexed by

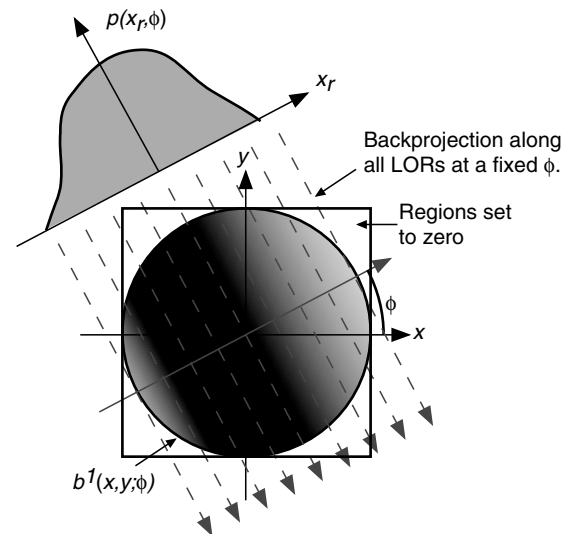


FIGURE 15 Backprojection into an image reconstruction array of all values of $p(x_r, \phi)$ for a fixed value of ϕ .

ϕ , with $x_r = x \cos \phi + y \sin \phi$. The full backprojection (see Eq. 21) is then formed by integration with respect to ϕ :

$$b(x, y) = \int_0^\pi b^1(x, y; \phi) d\phi \quad (23)$$

If we now consider the Fourier transform $B^1(v_x, v_y; \phi) = F_2 \{b^1(x, y; \phi)\}$, and

$$\begin{aligned} B^1(v_x, v_y; \phi) &= \int_{-\infty}^{\infty} \int_{-\infty}^{\infty} b^1(x, y; \phi) e^{-2\pi i(xv_x + yv_y)} dx dy \\ &= \int_{-\infty}^{\infty} \int_{-\infty}^{\infty} p(x_r, \phi) e^{-2\pi i(x_r v_{xr} + y_r v_{yr})} dx_r dy_r \\ &= P(v_{xr}, \phi) \delta(v_{yr}) \end{aligned} \quad (24)$$

where the last result holds if we assume $b^1(x, y; \phi)$ is constant in the y_r direction (that is, not truncated to the FOV). In other words, the Fourier transform of a single backprojection is nonzero along a line through the origin. Along the line, the values are equal to the Fourier transform of the projection (and thus the object via the central section theorem of Eq. 13), multiplied by the delta function in the perpendicular direction. This result (illustrated in Figure 16) is sometimes known as the backprojection theorem and is a corollary to the central section theorem.

If we perform backprojections at two angles, say ϕ_1 and ϕ_2 , and examine the Fourier transform of the result, we see that the contribution at the origin is doubled. In the limit of continuous sampling in ϕ we have:

$$\begin{aligned} B(v_x, v_y) &= \int_0^\pi B^1(v_x, v_y; \phi) d\phi \\ &= \int_0^\pi F(v_{xr}, v_{yr}) \delta(v_{yr}) d\phi \end{aligned} \quad (25)$$

To interpret Eq. (25) we regard v_x and v_y as parameters and $\delta(v_{yr}) = \delta(v_{yr}(\phi))$ using the inverse of Eq. (12). Then by taking advantage of the identity $\delta(f(x)) = \sum_i (\delta(x - x_i) / |f'(x_i)|)$, where x_i are the zeros of $f(x)$, we come to the important result:

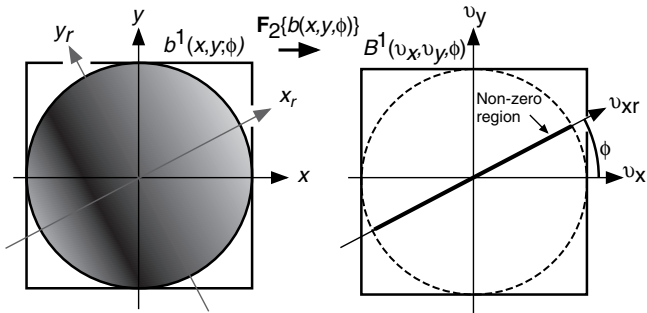


FIGURE 16 The Fourier transform of a backprojection at a single angle, $B^1(v_x, v_y; \phi)$, is equal to $P(v_{xr}, \phi) \delta(v_{yr})$, the Fourier transform of the projection, multiplied by the delta function in the perpendicular direction. If $p(x_r, \phi)$ is the projection of $f(x, y)$, then from the central section theorem (Eq. 13) we have $B^1(v_x, v_y; \phi) = F(v_{xr}, v_{yr}) \delta(v_{yr})$, with $v_{yr} = -v_x \sin \phi + v_y \cos \phi$.

$$B(v_x, v_y) = \frac{F(v_x, v_y)}{v} \quad (26)$$

where $v = \sqrt{v_x^2 + v_y^2}$ is the radial frequency-space variable. Equation (26) says that the two-dimensional Fourier transform of the backprojection is the Fourier transform of the object weighted by the inverse distance from the origin. This inverse distance weighting, which comes from the polar coordinate oversampling of the Fourier transform, is a characteristic of backprojecting parallel X-ray transform data and is thus applicable to PET, SPECT, and X-ray CT imaging, as well as many nonmedical imaging modalities.

By computing the inverse Fourier transform of Eq. (26) we have:

$$b(x, y) = f(x, y) * h(x, y) \quad (27)$$

where $*$ represents the appropriate convolution, which is two-dimensional in this case. Using the two-dimensional Fourier transform of a rotationally symmetric function, which is also known as the Hankel transform (Bracewell, 1965), the linear system response function is given by

$$h(x, y) = F_2^{-1} \left\{ \frac{1}{v} \right\} = \frac{1}{r} \quad (28)$$

where $r = \sqrt{x^2 + y^2}$. From Eq. (28) we see that the backprojection of X-ray transform data comprises a shift-invariant imaging system, as illustrated in Figure 17.

In imaging systems the linear system response function $h(x, y)$ is often called the point-response or point-spread function (PSF) because it describes the appearance of an ideal point-source object after the imaging process. Because the $1/v$ term in Eq. (26) amplifies low frequencies and attenuates high frequencies, the resulting output of the system in Figure 17 is a smoothed or blurred version of the input. Thus simple backprojection by itself is not sufficient for quantitatively accurate image reconstruction, and additional techniques must be employed to compensate for the $1/r$ blurring.

B. Reconstruction by Backprojection Filtering

Our goal is to compute $f(x, y)$ from $p(x_r, \phi)$, and an approach suggested by Eq. (26) is:

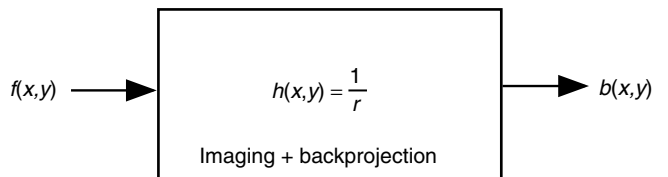


FIGURE 17 Illustration of combined imaging and backprojection as a linear shift-invariant system with $b(x, y) = f(x, y) * (1/r)$.

$$f(x, y) = F_2^{-1} \left\{ v F_2 \left\{ b(x, y) = \int_0^\pi p(x_r, \phi) d\phi \right\} \right\} \quad (29)$$

This is known as the backprojection filtering (BPF) image reconstruction method, in which the projection data are first backprojected, filtered in Fourier space with the cone filter $v = \sqrt{v_x^2 + v_y^2}$, and then inverse Fourier transformed. Alternatively, the filtering can be performed in image space via the convolution of $b(x, y)$ with $F_2^{-1}\{v\}$. A disadvantage of this approach is that the function $b(x, y)$ has a larger support than $f(x, y)$ due to the convolution with the $(1/r)$ term, which results in gradually decaying values outside the support of $f(x, y)$. Thus any numerical procedure must first compute $b(x, y)$ using a significantly larger image matrix size than is needed for the final result. This disadvantage can be avoided by interchanging the filtering and backprojection steps shown next.

C. Reconstruction by Filtered Backprojection

If we interchange the order of the filtering and backprojection steps in Eq. (29), we obtain the useful filtered backprojection (FBP) image reconstruction method:

$$f(x, y) = \int_0^\pi p^F(x_r, \phi) d\phi \quad (30)$$

where the filtered projection, given by

$$p^F(x_r, \phi) = F_1^{-1} \left\{ |v_{xr}| F_1 \{ p(x_r, \phi) \} \right\} \quad (31)$$

can be regarded as precorrected for the oversampling of the Fourier transform of $f(x, y)$. The one-dimensional ramp filter, $|v_{xr}|$, is a section through the rotationally symmetric two-dimensional cone filter $v = \sqrt{v_x^2 + v_y^2}$. The filtering step of Eq. (31) can also be performed by $p^F(x_r, \phi) = p(x_r, \phi) * h^{-1}(x_r)$, where the data-space version of the ramp filter, $h^{-1}(x_r)$, can be derived as (Kak and Slaney, 1988):

$$\begin{aligned} h^{-1}(x_r) &= F_1^{-1} \left\{ |v_{xr}| \right\} \\ &= \lim_{\epsilon \rightarrow 0} F_1^{-1} \left\{ |v_{xr}| e^{-\epsilon |v_{xr}|} \right\} \\ &= \lim_{\epsilon \rightarrow 0} \frac{\epsilon^2 - (2\pi x_r)^2}{\left(\epsilon^2 + (2\pi x_r)^2 \right)^2} \end{aligned} \quad (32)$$

With either form of filtering, the prefiltered projection will have negative tails outside the support of $f(x, y)$ due to the $-(2\pi x_r)^2$ term of Eq. (32) for large x_r . These tails remove the gradually decaying values outside the support of $f(x, y)$ that are otherwise present in a backprojection. An advantage of FBP is that the ramp filter is applied to each measured projection, which has a finite support in x_r , and we only need to backproject the filtered projections for $|x_r| \leq R_{\text{FOV}}$. This means that with FBP the image can be efficiently calculated with a much smaller reconstruction matrix than can be used with BPF for the same level of

accuracy. This is part of the reason for the popularity of the FBP algorithm.

A more direct, but perhaps less intuitive, derivation can be used to show that the ramp filter also arises from the Jacobian of the polar to rectangular sampling of the Fourier transform of the object. We start with the identity

$$f(x, y) = F_2^{-1} \left\{ F(v_x, v_y) \right\} = \int_{-\infty}^{\infty} \int_{-\infty}^{\infty} F(v_x, v_y) e^{i2\pi(xv_x + yv_y)} dv_x dv_y \quad (33)$$

By transforming to standard polar coordinates for the two-dimensional plane $\{(v, \phi) | 0 \leq v \leq \infty, 0 \leq \phi < 2\pi\}$ we have,

$$f(x, y) = \int_0^{2\pi} \int_0^\infty F(v, \phi) e^{i2\pi v(x \cos \phi + y \sin \phi)} v dv d\phi \quad (34)$$

An alternate span of the two-dimensional plane is given by $\{(v, \phi) | -\infty \leq v \leq \infty, 0 \leq \phi < \pi\}$, so we can change the limits of integration by using the symmetry relationship $F(v, \phi + \pi) = F(-v, \phi)$, but which requires $v dv \rightarrow |v| dv$, to obtain

$$f(x, y) = \int_0^\pi \int_{-\infty}^\infty F(v, \phi) e^{i2\pi v(x \cos \phi + y \sin \phi)} |v| dv d\phi \quad (35)$$

A key step is to recognize that $v = v_{xr}$, $x_r = x \cos \phi + y \sin \phi$, and $F(v, \phi) = P(v_{xr}, \phi)$ (by the central section theorem), which allow us to write:

$$f(x, y) = \int_0^\pi \int_{-\infty}^\infty |v_{xr}| P(v_{xr}, \phi) e^{i2\pi x_r v_{xr}} dv_{xr} d\phi \quad (36)$$

which is equivalent to Eq. (30).

We note that although Eq. (36) is correct as a continuous inversion formula, a direct discrete implementation of the ramp filter term as given by Eqs. (30) and (36) will, however, introduce a subtle problem with the removable singularity at $v_{xr} = 0$ because the filtered projection must necessarily have a zero average value. This, in turn, means that $\iint f(x, y) dx dy = 0$, which is clearly incorrect if, for example, $f(x, y)$ is a density function such that $f(x, y) \geq 0$ everywhere. This situation can be avoided in discrete implementations by calculating the filter function in image space (Kak and Slaney, 1988) or by careful calculation of residual offset terms to be applied to the ramp filter in frequency space (O'Sullivan, 1985).

1. Relation of Filtered Backprojection to the Inverse Radon Transform

We can explicitly relate the FBP solution of Eq. (36) to the inverse Radon transform, by use of the derivative theorem for Fourier transforms, that is $\mathcal{F}_1\{f'(x)\} = i2\pi v F(v)$, and the definition of $|x| = x \text{sgn}(x)$, where $\text{sgn}(x)$ (or the signum function) is defined as

$$\text{sgn}(x) = \begin{cases} 1 & x > 0 \\ -1 & x < 0 \end{cases} \quad (37)$$

and has a Fourier transform of

$$F_1\{\text{sgn}(x)\} = \frac{i}{\pi v_{xr}} \quad (38)$$

We can then write Eq. (36) as

$$\begin{aligned} f(x, y) &= \int_0^\pi \left[F_1^{-1}\{\text{sgn}(v_{xr}) v_{xr} P(v_{xr}, \phi)\} \right] d\phi \\ &= \int_0^\pi \left[F_1^{-1}\{\text{sgn}(v_{xr})\} * F_1^{-1}\{v_{xr} P(v_{xr}, \phi)\} \right] d\phi \end{aligned} \quad (39)$$

and by computing the inverse Fourier transforms we have

$$f(x, y) = \frac{-1}{2\pi^2} \int_0^\pi \left[\frac{1}{x_r} * \frac{\partial p(x_r, \phi)}{\partial x_r} \right] d\phi \quad (40)$$

which is the inverse Radon transform, although a different approach was used by Radon (Deans, 1983). These results show that the solution to the inverse X-ray transform (in two dimensions) can be arrived at through several different routes. The use of the central section theorem, however, leads to the most insight about the nature of how the X-ray transform samples the Fourier transform of the object, as explicitly illustrated in Figure 18 for the discrete sampling that occurs in practice. For the discrete sampling shown in Figure 18, we can see that in the limit as $\Delta v_{xr} \rightarrow 0$ and $\Delta\phi \rightarrow 0$, the density of sampling of $F(v_x, v_y)$ varies as $1/v$, resulting in Eq. (26).

D. Reconstruction by Direct Fourier Methods

An alternate approach suggested by Figure 18 is directly interpolating from the polar sampling of the Fourier transform

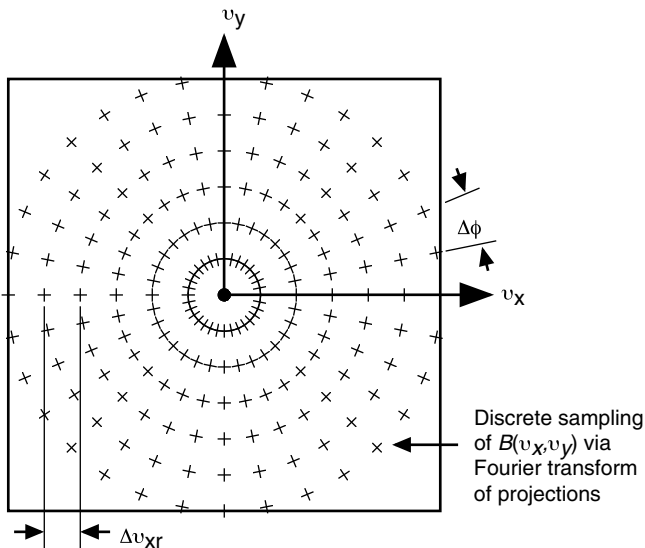


FIGURE 18 The discrete sampling pattern of $F(v_x, v_y)$ contained in $B(v_x, v_y)$, resulting from the use of discretely sampled projections.

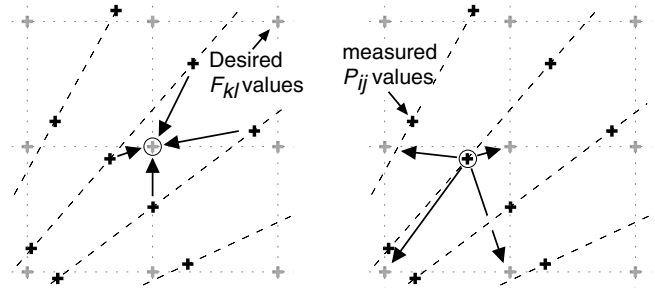


FIGURE 19 Image reconstruction by direct interpolation in the Fourier domain. For normal interpolation the nearest measured data values are pulled via interpolation to a desired grid point. In gridding, measured data values are pushed (also via interpolation) to the nearest rectangular grid points.

supplied by $P_{ij} = P(i\Delta v_{xr}, j\Delta\phi)$ to a rectangular sampling $F_{kl} = F(k\Delta v_x, l\Delta v_y)$ suitable for inverse discrete Fourier transforms, namely the fast Fourier transform (FFT). There are two possible approaches for this interpolation, which are illustrated in Figure 19. Using standard interpolation methods, the value at a desired rectangular grid point F_{kl} is estimated or pulled via interpolation from the nearest measured polar grid points P_{ij} . This approach makes poor use of the available data because, close to the origin, measured data points go unused.

In the gridding approach, each measured data point is pushed (via interpolation) to the nearest rectangular grid points, thus ensuring equal use of all measured data. To correct for the nonuniform sampling of $F(v_x, v_y)$ (described by Eq. 26), however, it is necessary to apply the cone filter $v = \sqrt{v_x^2 + v_y^2}$ to the gridded data. In addition, the accuracy of the reconstructed image depends strongly on the quality of the interpolation method, and unless the interpolation method is carefully chosen the resulting images will be less accurate or slower to compute than those produced by FBP (O'Sullivan, 1985). An interesting adjunct to the interpolation method is the use of alternative interpolating functions. With the standard contiguous pixel interpolating functions, the support of image space representation is finite, nonoverlapping, contiguous and easy to calculate and represent, but at the expense of an infinite and slowly decaying support in frequency-space. An alternative approach is to use basis functions that are constrained in extent and amplitude in both spaces. One such set of functions that have been shown to be very useful for interpolation methods are the modified Kaiser-Bessel (MKB) functions (Lewitt, 1992). If the direct Fourier method is implemented with gridding and carefully chosen MKB basis functions, then more accurate images can be produced in less time than with FBP algorithms. It should be noted, however, that FBP remains the most common method of image reconstruction due to its combination of accuracy (particularly with low-noise projection data), speed of computation, and simplicity of implementation.

E. Other Data Acquisition Formats

1. List Mode

The reconstruction methods considered so far are based on parallel X-ray transform projections in two dimensions. There are, however, other possible data acquisition formats, the most straightforward of which is list mode. In the list mode format, the LOR of each event is separately recorded in turn, possibly with other information, such as the time and photon energy. This is an efficient form of storage for otherwise sparse data histograms (that is, few photon events and many potential LORs), but it is not amenable to analytic reconstruction methods such as FBP without first histogramming the list-mode data into a standard sinogram or projection data format, which can be an inefficient procedure. Alternatively, each list-mode event can be backprojected into a reconstruction matrix, which is an efficient means of data storage but incurs the disadvantages of the BPF approach as previously discussed. For this reason, and because of the typically high levels of statistical noise, iterative methods are often used to reconstruct list-mode data.

2. Linograms

For FBP, the reconstruction of a point in the image is described by the integral along a sinusoid in the filtered sinogram (Figure 4b and Eq. 30); thus, two-dimensional backprojection involves a complex set of interpolations. An alternate approach was proposed by Edholm (1987), whose first insight for the linogram method was to choose “natural” parameters (u, v) to index a LOR for a pair of linear detectors, as shown in Figure 20(a), rather than the conventional parameters used for a circular tomograph. In the linogram acquisition format, all LORs passing through a point in the FOV lie on a straight line in the data space (Figure 20b), thus the term *linogram* for the data format.

The backprojection of all the LORs passing through a point in the (x_0, y_0) in the image will then correspond to integration along a straight line in the linogram, which is a

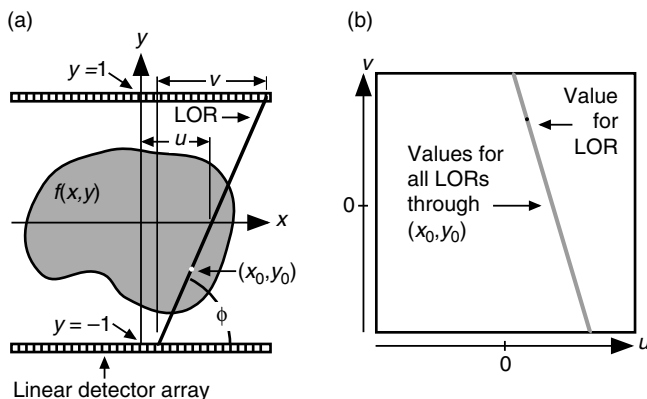


FIGURE 20 The linogram format. (a) Data acquisition with parallel linear detector arrays. (b) In the linogram data format, all LORs passing through a point (x_0, y_0) lie on a straight line in the data space.

simpler interpolation problem than the backprojection of sinograms. The next step is to note that integration along a set of parallel lines through the linogram will backproject the corresponding set of image points. Edholm's second insight was that to backproject such a set of points, the integration along the parallel lines through the linogram can be replaced by a section through the origin of the two-dimensional Fourier transform of the linogram. In other words we can take the unusual step of applying the two-dimensional central section theorem to the data space rather than to image space. The result is a fast and accurate method of two-dimensional backprojection using only Fourier transforms (Edholm and Herman, 1987; Edholm *et al.*, 1988; Magnusson, 1993). A disadvantage of the linogram method is that to adequately sample the object, the data must be collected from at least one more detector position, typically rotated by 90° so the linear detector arrays are parallel to the y -axis at $x = \pm 1$. This produces two linogram data sets, each of which must be filtered with the ramp filter, backprojected, and then summed.

3. Fan Beam

For many imaging modalities, such as X-ray CT or cardiac SPECT imaging, collecting parallel LOR data is relatively inefficient. In these situations using a fan-beam acquisition geometry (Figure 21) provides more efficient or higher resolution acquisitions.²

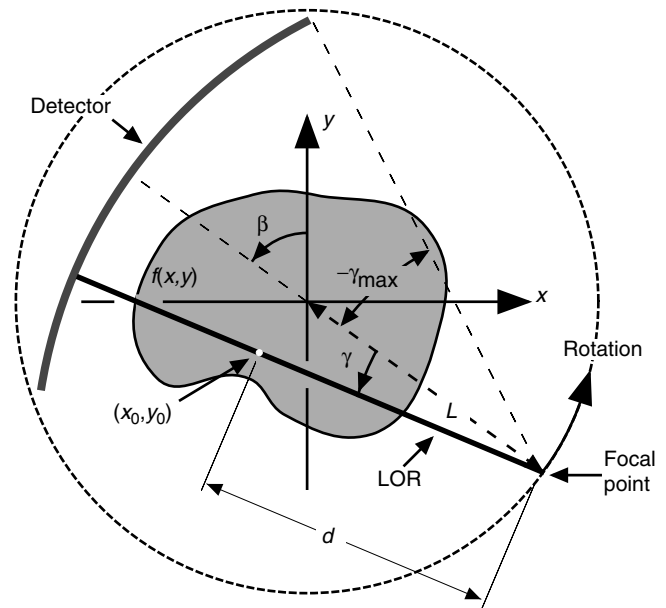


FIGURE 21 Fan-beam acquisition format in which each LOR is parameterized by two angles: the focal point angle $0 \leq \beta < 2\pi$ and the fan angle $-\gamma_{\max} \leq \gamma \leq \gamma_{\max}$. The focal point, which can correspond to the focal point of a SPECT collimator or the X-ray source for a CT scanner, rotates with the detector.

²For a circular PET tomograph, the native data format is actually fan beam, although it is almost always treated as parallel beam.

For $0 \leq \beta < 2\pi$ and $-\gamma_{\max} \leq \gamma \leq \gamma_{\max}$, individual LORs from a fan-beam projection $p(\gamma, \beta)$ correspond to LORs from a parallel-beam projection $p(x_r, \phi)$, where $x_r = -L \sin \gamma$ and $\phi = \beta + \gamma$ so there is clearly sufficient data to reconstruct $f(x, y)$. To reconstruct $f(x, y)$ from $p(\gamma, \beta)$, we use a change in variables for fan-beam projections in the convolution-backprojection version of Eqs. (30) and (31), with $0 \leq \phi < 2\pi$ and $-x_{r,\max} \leq x_r \leq x_{r,\max}$, where $x_{r,\max} = -L \sin \gamma_{\max}$:

$$f(x, y) = \frac{1}{2} \int_0^{2\pi} \int_{-x_{r,\max}}^{x_{r,\max}} h^{-1}(x \cos \phi + y \sin \phi - x_r') p(x_r', \phi) dx_r' d\phi \quad (41)$$

Using polar coordinates $x = r \cos \alpha$ and $y = r \sin \alpha$,

$$f(r, \alpha) = \frac{1}{2} \int_0^{2\pi} \int_{-x_{r,\max}}^{x_{r,\max}} h^{-1}(r \cos(\phi - \alpha) - x_r') p(x_r', \phi) dx_r' d\phi \quad (42)$$

Using $x_r' = -L \sin \gamma'$ and $\phi = \beta + \gamma'$, and after some simplification, we have:

$$f(r, \alpha) = \frac{1}{2} \int_0^{2\pi} \int_{-\gamma_{\max}}^{\gamma_{\max}} h^{-1}(r \cos(\beta + \gamma' - \alpha) + L \sin \gamma') p(-L \sin \gamma', \beta + \gamma') L \cos \gamma' d\gamma' d\beta \quad (43)$$

For a fixed point (x_0, y_0) located at distance d along the LOR indexed by β and γ , we can use the relation $r \cos(\beta + \gamma' - \alpha) + L \sin \gamma' = d \sin(\gamma' - \gamma)$ and from Eq. (32) we can show that $h^{-1}(d \sin \gamma) = (\gamma/d \sin \gamma)^2 h^{-1}(\gamma)$, so if we recognize that $p(x_r = -L \sin \gamma', \phi = \beta + \gamma') = p(\gamma, \beta)$ for the specific LOR, we can write Eq. (43) as convolution followed by a distance-weighted back-projection:

$$f(r, \alpha) = \int_0^{2\pi} \frac{p^F(\gamma, \beta)}{d^2} d\beta \quad (44)$$

where $p^F(\gamma, \beta) = (p(\gamma, \beta) \cdot L \cos \gamma) * ((\gamma/\sqrt{2} \sin \gamma)^2 \cdot h^{-1}(\gamma))$.

With the advent of helical scanning protocols for fan-beam CT systems (during which there is both continuous motion of the patient through the scanner and rotation of the X-ray-detector assembly), there have been several advances made in helical/fan-beam reconstruction algorithms. Further information can be found in recent conference proceedings of the 3D Meetings ("1991 International Meeting," 1992; "1993 International Meeting," 1994; "1995 International Meeting," 1996; "1997 International Meeting," 1998; "1999 International Meeting," 2001; "2001 International Meeting," 2002) and the conference proceedings of the IEEE NSS/MIC meetings.

F. Regularization

The inverse problem of Eq. (4) is ill-posed, and its solution, (Eq. 36), is unstable in the sense that a small perturbation of the data, $p(x_r, \phi)$, can lead to an unpredictable change in the estimate of $f(x, y)$. Because photon detection is a stochastic process, some form of regularization is required

to constrain the solution space to physically acceptable values.

The most common form of regularizing image reconstruction is via simple smoothing. With the FBP algorithm, Eq. (36), this can be written as

$$f(x, y) \approx \tilde{f}(x, y) = \int_0^{x_{r,\max}} \int_{-\infty}^{\infty} W(v_{xr}) |v_{xr}| P(v_{xr}, \phi) e^{i2\pi x_r v_{xr}} dv_{xr} d\phi \quad (45)$$

where $\tilde{f}(x, y)$ is the reconstructed estimate of $f(x, y)$ and $W(v_{xr})$ is the apodizing (or smoothing) function. In the tomographic image reconstruction literature, the term *filter* is reserved for the unique ramp filter, $|v_{xr}|$, that arises from the sampling of the Fourier transform of the object (Figure 18). In other words, for two-dimensional image reconstruction there is only one possible filter (the ramp filter), whereas the apodizing function can take on any shape that is deemed most advantageous based on image SNR or other considerations. Note that unless $W(v_{xr}) = 1$, Eq. (45) yields a biased estimate of $f(x, y)$.

A simple model explains the principle of most apodizing functions. If we regard the measured projection data as the sum of the true projection data and uncorrelated random noise, that is $p^M(x_r, \phi) = p(x_r, \phi) + n(x_r, \phi)$, then the corresponding measured power spectrum is $P_{p^M}(v_{xr}, \phi) = P_p(v_{xr}, \phi) + P_n(v_{xr}, \phi)$. With the finite frequency response of the detection system, the signal power, $P_p(v_{xr}, \phi)$, will gradually roll off, whereas the noise power for $P_n(v_{xr}, \phi)$ will remain essentially constant, as illustrated in Figure 22. The effect of the ramp filter, also shown in Figure 22, will be to amplify the high-frequency components of the power spectrum, which are dominated by noise at increasing frequencies. The use of a cosine apodizing window (also called a Von Hann, Hann, or Hanning window) is given by

$$W(v_{xr}) = \begin{cases} \frac{1}{2} \left(1 - \cos \left(\frac{\pi v_{xr}}{v_c} \right) \right), & |v_{xr}| < v_c \\ 0, & |v_{xr}| \geq v_c \end{cases} \quad (46)$$

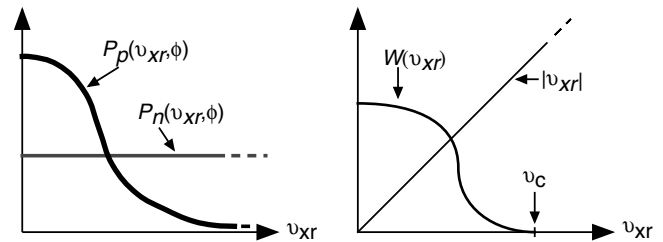


FIGURE 22 Illustration of the use of an apodized ramp filter $W(v_{xr})|v_{xr}|$ to suppress amplification of high-frequency noise power above the cutoff frequency v_c , where $P_n(v_{xr}, \phi) > P_p(v_{xr}, \phi)$.

where v_c is a predetermined cut-off frequency. The specific shape of $W(v_{xr})$ will determine the noise/resolution trade-offs in the reconstructed image and also affect the noise covariance (noise texture) in the image. In practice it is difficult to rigorously justify a choice of $W(v_{xr})$. In principle, at least, $W(v_{xr})$ should be chosen to optimize a specific task, such as lesion detection.

V. THREE-DIMENSIONAL IMAGE RECONSTRUCTION FROM X-RAY PROJECTIONS

There are two important differences between two-dimensional and three-dimensional image reconstruction from X-ray transforms: the spatially varying scanner response and data redundancy. The data redundancy we have already noted in Section IIIB2 with the discussion of the set Ω_Θ (Figure 12), and we devote most of the remainder of this chapter to this subject, after discussing the spatial variance aspects. With our current understanding of two-dimensional image reconstruction, there are several different routes to understanding fully three-dimensional image reconstruction. We start with a straightforward extension of the two-dimensional results and then show how the data redundancy opens up many more possible methods of three-dimensional image reconstruction.

A. Spatial Variance and the Three-Dimensional Reprojection Algorithm

The spatially varying scanner response can be understood as the consequence of the finite axial extent of the scanner, leading to truncated projections (see Figure 7). In a two-dimensional ring scanner, the observed intensity of a point source, expressed as

$$I = \int_0^\pi \int_{-\infty}^\infty p(x_r, \phi) dx_r d\phi \quad (47)$$

remains approximately constant, regardless of the position of the point source inside the scanner's FOV, as illustrated in Figure 23. For a three-dimensional cylindrical scanner, however, with truncated projections $p^T(x_r, y_r, \phi, \theta)$, the observed intensity of a point source

$$I = \int_{-\Theta}^\Theta \int_0^\pi \int_{-\infty}^\infty \int_{-\infty}^\infty p^T(x_r, y_r, \phi, \theta) dx_r dy_r d\phi \cos \theta d\theta \quad (48)$$

varies depending on the position of the point source inside the scanner's FOV, particularly as the point source moves axially (Figure 23). For the impractical case of a nontruncated spherical scanner ($\Theta = \pi/2$), the scanner's response would be spatially invariant, although the issue of data redundancy would remain.

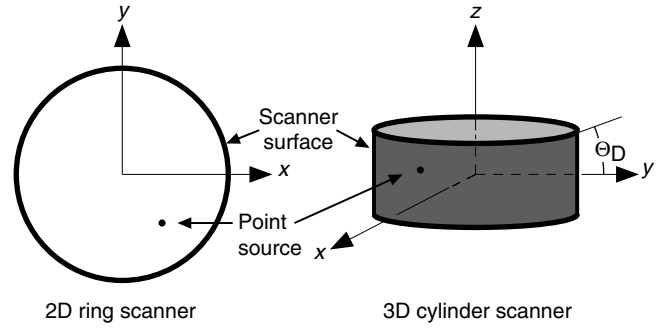


FIGURE 23 Illustration of the spatial invariance of two-dimensional imaging with X-ray transforms and the spatial variance of three-dimensional imaging with X-ray transforms. For the three-dimensional cylindrical scanner, the observed intensity of the point source varies depending on the position of the point source inside the scanner's FOV.

The spatially varying nature of the measured data complicates the image reconstruction process. For example, if regions of the support of $p(x_r, y_r, \phi, \theta)$ are unmeasured due to truncation (Figure 7), then accurately computing the two-dimensional Fourier transform of the projection, say for an FBP type of algorithm, is not possible by simply using FFTs.

A common method of restoring spatial invariance to measured three-dimensional X-ray projection data is the three-dimensional reprojection (3DRP) algorithm (Kinahan and Rogers, 1989). In this method, unmeasured regions of projections are estimated by numerically forward-projecting through an initial estimate of the image. The initial estimate is formed by reconstructing an image using the direct planes $p^T(x_r, y_r, \phi, \theta = 0)$ that are not truncated using two-dimensional FBP for each transverse plane. Further details on the implementation of this algorithm are given in Defrise and Kinahan (1998).

It is also possible to restrict the polar angle range to $|\theta| \leq \Theta_{\text{FOV}} < \Theta_D$ (Figure 7), that is, use only those projections that are not truncated. For medical imaging systems, however, this is usually not helpful because the patient extends the entire axial length of the scanner, ($H_{\text{FOV}} = H_D$ in Figure 7), so that $\Theta_{\text{FOV}} = 0$. However, by using either the 3DRP algorithm or restricting $|\theta| \leq \Theta_{\text{FOV}} < \Theta_D$, we assume that the projections are not truncated for the remainder of this chapter and that the set of complete projections correspond to the set Ω_Θ in Figure 12.

B. Three-Dimensional Backprojection.

Three-dimensional backprojection is analogous to the two-dimensional case (Eq. 21), and the backprojected image is given by,

$$b(x, y, z) = \int_{-\Theta}^\Theta \int_0^\pi p(x_r, y_r, \phi, \theta) d\phi \cos \theta d\theta \quad (49)$$

Similar to the two-dimensional backprojection case, it is typically more efficient to backproject a two-dimensional view at a fixed direction (ϕ, θ) , by placing the values of $p(x_r, y_r, \phi, \theta)$ back into a three-dimensional image array along the appropriate LORs. This can be expressed for a single view as:

$$b^1(x, y, z; \phi, \theta) = p(x_r, y_r, \phi, \theta) \quad (50)$$

The full backprojection (Eq. 49) is then formed by integration with respect to ϕ and θ :

$$b(x, y, z) = \int_{-\Theta}^{\Theta} \int_0^{\pi} b^1(x, y, z; \phi, \theta) d\phi \cos \theta d\theta \quad (51)$$

The three-dimensional backprojection is considerably more computationally intensive than the two-dimensional backprojection due to two factors: There is an extra level of interpolation in the axial direction implied by Eq. (50) (compared to Eq. 22) and there is the additional integration over the co-polar angle θ in Eq. (51) (compared to Eq. 23).

To develop some understanding of $b(x, y, z)$, analogous to two-dimensional backprojection, we start by deriving the three-dimensional version of the backprojection theorem by considering the Fourier transform of the backprojection of a single view

$$\begin{aligned} B^1(v_x, v_y, v_z; \phi, \theta) &= \int_{-\infty}^{\infty} \int_{-\infty}^{\infty} \int_{-\infty}^{\infty} b^1(x, y, z; \phi, \theta) e^{-2\pi i(xv_x + yv_y + zv_z)} \\ &\quad dx dy dz \quad (52) \\ &= \int_{-\infty}^{\infty} \int_{-\infty}^{\infty} \int_{-\infty}^{\infty} p(x_r, y_r, \phi, \theta) e^{-2\pi i(x_r v_x + y_r v_y + z_r v_z)} \\ &\quad dx_r dy_r dz_r \\ &= P(v_x, v_y, v_z, \phi, \theta) \delta(v_z) \end{aligned}$$

where we assume $b^1(x, y, z; \phi, \theta)$ is constant in the z_r direction (that is, not truncated to the FOV). Thus the Fourier transform of a single backprojection is nonzero along a plane through the origin. Along the plane the values are equal to the Fourier transform of the projection (and thus the object via the central section theorem of Eq. 16), multiplied by the delta function in the perpendicular direction.

For the full backprojection $b(x, y, z)$ we can substitute Eq. (52) into Eq. (51) (similar to Eq. 25); this result was first derived by Colsher (1980). The result is more simply expressed in the frequency space spherical coordinates, $\mathbf{u} = (v, \phi, \psi)$, shown in Figure 24, and is given by

$$B(v, \phi, \psi) = F(v, \phi, \psi) H(v, \phi, \psi) \quad (53)$$

where $F(v, \phi, \psi)$ is the 3D Fourier transform of the object in spherical coordinates and $H(v, \phi, \psi) = H(v, \psi)$ is the three-dimensional Fourier transform of the rotationally symmetric PSF, which has different behavior in the two regions indicated in Figure 24.

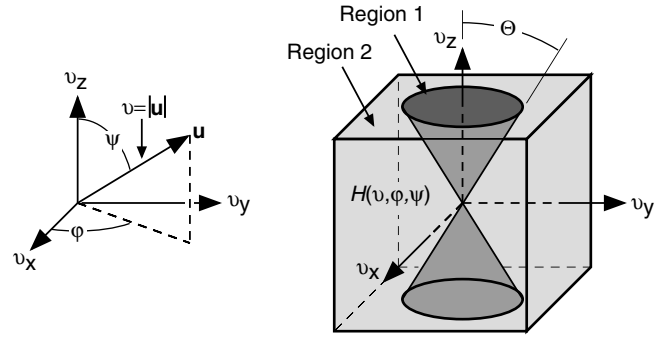


FIGURE 24 Frequency space spherical coordinates, $\mathbf{u} = (v, \phi, \psi)$, and illustration of the two regions for the different behavior of the PSF, $H(v, \phi, \psi)$, arising from the backprojection of three-dimensional X-ray projection data Ω_Θ in Figure 12.

$$H(v, \psi) = \begin{cases} \frac{2\pi}{v} & \text{Region 1: } |\psi| \leq \Theta \\ 4 \sin^{-1} \left(\frac{\sin \Theta}{|\sin \psi|} \right) \frac{1}{v} & \text{Region 2: } |\psi| > \Theta \end{cases} \quad (54)$$

Similar to the two-dimensional case of Eq. (28), the three-dimensional backprojection is similar to a low pass filtering as a result of the $v^{-1} = |\mathbf{u}|^{-1}$ term in Eq. (54), and the backprojected image is a blurred version of the original object. The form of Eq. (54) can be understood by considering the three-dimensional version of the central section theorem for the X-ray projections (Eq. 16) in conjunction with the set of measured projections given by Ω_Θ (Figure 12). We derive Eq. (54) by using the filter equation, which gives more insight into the form of the blurring function. We can note however, that in the limit as $\Theta \rightarrow \pi/2$ Eq. (54) reduces to $H(v, \psi) = H(v) = 1/v$, corresponding to the (impractical) case of a spherical scanner system. As $\Theta \rightarrow 0$, which corresponds to Ω_0 (Figure 12) for a multiplane scanner acquiring only two-dimensional data with each imaging plane, Eq. (54) reduces to $H(v, \psi) = 1/(v|\sin \psi|) = 1/\sqrt{v_x^2 + v_y^2}$, which corresponds to the two-dimensional case of Eq. (26). In other words, in Region 1 the oversampling of the backprojected image varies inversely as the distance from the origin, whereas in Region 2 the oversampling varies inversely as the distance from the v_z -axis. Thus the sampling of the Fourier transform of the object is determined by the data acquisition.

C. Three-Dimensional Reconstruction by Backprojection Filtering

The approach followed by Colsher (1980) was to develop a three-dimensional BPF image reconstruction algorithm by solving Eq. (53) for $F(\mathbf{u})$,

$$F(v, \phi, \psi) = B(v, \phi, \psi) G_c(v, \psi) \quad (55)$$

where $G_c(v, \psi)$ is the Colsher reconstruction filter defined by

$$G_c(v, \psi) = \frac{1}{H(v, \psi)} \quad (56)$$

From Eq. (54) we see that $G_c(v, \psi)$ has ramp-type behavior similar to the two-dimensional reconstruction filter. The BPF algorithm implied by Eq. (55) is thus

$$f(\mathbf{x}) = F_3^{-1} \left\{ G_c(v, \psi) F_3 \left\{ \int_{-\Theta}^{\Theta} \int_0^{\pi} p(x_r, y_r, \phi, \theta) d\phi \cos \theta d\theta \right\} \right\} \quad (57)$$

where the filtering by multiplication with $G_c(v, \psi)$ can be replaced by a convolution in image space with $F_3^{-1}\{G_c(v, \psi)\}$. With either approach, the filtering step can be seen as compensating for the sampling of the Fourier transform of $F(\mathbf{u})$ that is imposed by the collection of the X-ray transform data.

As in the two-dimensional case, the ramp filter term in Eq. (56) introduces a removable singularity at $v = 0$ because the filtered image has a zero average value. This situation can be avoided in discrete implementations by calculating the filter function in image space (Kinahan *et al.*, 1988; Defrise *et al.*, 1993), although this is considerably more complicated than for the two-dimensional case, or by over-sampling the filter in frequency space (Stearns *et al.*, 1994).

The implementation of Eq. (57) has the same difficulties as the two-dimensional BPF algorithm (Eq. 29); that is, the projection data must be backprojected into a much larger reconstruction volume than is needed for the final image volume. As in the two-dimensional case, this disadvantage can be avoided by interchanging the filtering and back-projection steps.

D. Three-Dimensional Reconstruction by Filtered Backprojection

We can rewrite Eq. (57) as a FBP algorithm by interchanging the backprojection and filtering steps,

$$f(\mathbf{x}) = \iint_{\Omega_\Theta} F_2^{-1} \{ P(v_{xr}, v_{yr}, \phi, \theta) G(v_{xr}, v_{yr}, \phi, \theta) \} d\phi \cos \theta d\theta \quad (58)$$

where $G(v_{xr}, v_{yr}, \phi, \theta)$ can be regarded as a two-dimensional filter $G(v_{xr}, v_{yr})$ that varies with the projection and backprojection direction (ϕ, θ) . For the Colsher filter, $G_c(v_{xr}, v_{yr}, \phi, \theta)$ can be derived using the central section theorem (Figure 15) by taking a two-dimensional section through the origin of $G_c(v, \psi)$ (Eq. 54) at the appropriate angle.

The filter used in three-dimensional image reconstruction can have forms other than the Colsher filter given in Eq. (56) and in addition, as we show next, the class of filters for FBP is more general than for BPF. In other words, for the three-dimensional X-ray transform the reconstruction filter is not unique, and FBP filters allow for the most general form

(Clack, 1992). We show this through the use of the filter equation.

1. Filter Equation for the Three-Dimensional X-ray Transform

The filter equation is concisely derived using vector notation (Defrise *et al.*, 1989) to parameterize the line-integrals first described by Eq. (6):

$$p(\mathbf{s}, \hat{\mathbf{z}}_r) = \int_{-\infty}^{\infty} f(\mathbf{x} + \alpha \hat{\mathbf{z}}_r) d\alpha \quad (59)$$

where $\hat{\mathbf{z}}_r \in \Omega_\Theta$ (Figure 12), and $\mathbf{s} \in \hat{\mathbf{z}}_r^\perp$ such that $\mathbf{s} \in \mathbb{R}^3$ and $\mathbf{s} \cdot \hat{\mathbf{z}}_r = 0$. We note that $p(\mathbf{s}, \hat{\mathbf{z}}_r) = p(\mathbf{s}, -\hat{\mathbf{z}}_r)$. With this notation the central section theorem can be expressed as:

$$F(\mathbf{u}) = \iiint_{\mathbb{R}^3} f(\mathbf{x}) e^{-i2\pi(\mathbf{x} \cdot \mathbf{u})} d\mathbf{x} = P(\mathbf{u}, \hat{\mathbf{z}}_r) \quad (60)$$

where $P(\mathbf{u}, \hat{\mathbf{z}}_r)$ is the two-dimensional Fourier transform of the projection in direction $\hat{\mathbf{z}}_r$

$$P(\mathbf{u}, \hat{\mathbf{z}}_r) = \iint_{\mathbf{s} \cdot \hat{\mathbf{z}}_r = 0} p(\mathbf{s}, \hat{\mathbf{z}}_r) e^{-i2\pi(\mathbf{s} \cdot \mathbf{u})} d\mathbf{s} \quad (61)$$

and where \mathbf{u} is constrained to lie on the plane $\mathbf{u} \cdot \hat{\mathbf{z}}_r = 0$.

Starting from Eqs. (51) and (55) we have the reconstructed estimate of the Fourier transform of the object, $\tilde{F}(\mathbf{u})$,

$$F(\mathbf{u}) \approx \tilde{F}(\mathbf{u}) = B(\mathbf{u})G(\mathbf{u}) = \iint_{\Omega_\Theta} B^1(\mathbf{u}; \hat{\mathbf{z}}_r) G(\mathbf{u}) d\hat{\mathbf{z}}_r \quad (62)$$

and by using the three-dimensional backprojection theorem, Eq. (52),

$$\tilde{F}(\mathbf{u}) = \iint_{\Omega_\Theta} P(\mathbf{u}, \hat{\mathbf{z}}_r) \delta(v_z) G(\mathbf{u}) d\phi \cos \theta d\theta \quad (63)$$

Recognizing that $v_z = \mathbf{u} \cdot \hat{\mathbf{z}}_r$, we can write $\delta(\mathbf{u} \cdot \hat{\mathbf{z}}_r) G(\mathbf{u}) = \delta(\mathbf{u} \cdot \hat{\mathbf{z}}_r) G^1(\mathbf{u}; \hat{\mathbf{z}}_r)$, where for the function $G^1(\mathbf{u}; \hat{\mathbf{z}}_r)$ the vector \mathbf{u} is restricted to $\hat{\mathbf{z}}_r^\perp = \{\mathbf{u} \in \mathbb{R}^3 | \mathbf{u} \cdot \hat{\mathbf{z}}_r = 0\}$. In other words $G^1(\mathbf{u}; \hat{\mathbf{z}}_r)$ is zero except on the plane $\mathbf{u} \cdot \hat{\mathbf{z}}_r = 0$. With this change we have

$$\tilde{F}(\mathbf{u}) = \iint_{\Omega_\Theta} P(\mathbf{u}, \hat{\mathbf{z}}_r) \delta(\mathbf{u} \cdot \hat{\mathbf{z}}_r) G^1(\mathbf{u}; \hat{\mathbf{z}}_r) d\phi \cos \theta d\theta \quad (64)$$

As in Eq. (58), the function $G^1(\mathbf{u}; \hat{\mathbf{z}}_r)$ used in FBP can be regarded as a two-dimensional filter that varies with the projection and backprojection direction $\hat{\mathbf{z}}_r(\phi, \theta)$. This is actually a more general form than $G(\mathbf{u})$ used in BPF (Clack, 1992). From Eq. (60) we have $P(\mathbf{u}, \hat{\mathbf{z}}_r) = F(\mathbf{u})$ on the plane $\mathbf{u} \cdot \hat{\mathbf{z}}_r = 0$

$$\begin{aligned} \tilde{F}(\mathbf{u}) &= \iint_{\Omega_\Theta} F(\mathbf{u}) \delta(\mathbf{u} \cdot \hat{\mathbf{z}}_r) G^1(\mathbf{u}; \hat{\mathbf{z}}_r) d\phi \cos \theta d\theta \\ &= F(\mathbf{u}) \iint_{\Omega_\Theta} \delta(\mathbf{u} \cdot \hat{\mathbf{z}}_r) G^1(\mathbf{u}; \hat{\mathbf{z}}_r) d\phi \cos \theta d\theta \\ &= F(\mathbf{u}) T_G(\mathbf{u}) \end{aligned} \quad (65)$$

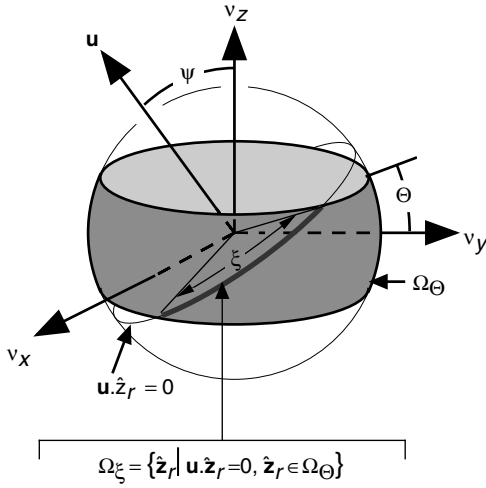


FIGURE 25 The Orlov sphere showing the set of directions of measured projections Ω_Θ and the set Ω_ξ of projections that contribute to the point \mathbf{u} .

where $T_G(\mathbf{u})$ is the transfer function of the linear system of measured projections followed by FBP reconstruction using the filter $G^1(\mathbf{u}; \hat{\mathbf{z}}_r)$. The reconstruction filter provides an accurate result if $\tilde{F}(\mathbf{u}) = F(\mathbf{u})$, which gives the filter equation (Defrise *et al.*, 1989):

$$T_G(\mathbf{u}) = \iint_{\Omega_\Theta} \delta(\mathbf{u} \cdot \hat{\mathbf{z}}_r) G^1(\mathbf{u}; \hat{\mathbf{z}}_r) d\hat{\mathbf{z}}_r = 1 \quad (66)$$

for all $\mathbf{u} \in R^3$.

The meaning of the filter equation is illustrated in Figure 25. For a given point in frequency space, \mathbf{u} , the delta function in Eq. (66) selects the set $\Omega_\xi = \{\hat{\mathbf{z}}_r | \mathbf{u} \cdot \hat{\mathbf{z}}_r = 0, \hat{\mathbf{z}}_r \in \Omega_\Theta\}$ of projection direction vectors within the measured set Ω_Θ that are perpendicular to \mathbf{u} . This represents the range of the measured projections that contribute to \mathbf{u} , or to any point along the line containing \mathbf{u} . This range is represented by ξ , the arc length of the great circle perpendicular to $\hat{\mathbf{z}}_r$ that intersects Ω_Θ . In other words, it represents the sampling density of the Fourier transform of the object at the point \mathbf{u} , and the filter $G^1(\mathbf{u}; \hat{\mathbf{z}}_r)$ compensates for this, resulting in proper normalization of the sampling density of the Fourier transform of the object.

As a specific example of a valid filter, we assume that $G^1(\mathbf{u}; \hat{\mathbf{z}}_r) = G(\mathbf{u})$, that is, the filter for a direction $\hat{\mathbf{z}}_r$ is a central section perpendicular to $\hat{\mathbf{z}}_r$ though $G(\mathbf{u})$ and that there is no additional dependence on direction. In that case, we have, where $(\iint_{\Omega_\Theta} \delta(\mathbf{u} \cdot \hat{\mathbf{z}}_r) d\phi \cos \theta d\theta) > 0$:

$$\begin{aligned} G(\mathbf{u}) &= \frac{1}{\iint_{\Omega_\Theta} \delta(\mathbf{u} \cdot \hat{\mathbf{z}}_r) d\phi \cos \theta d\theta} \\ &= \frac{|\mathbf{u}|}{\iint_{\Omega_\Theta} \delta(\hat{\mathbf{u}} \cdot \hat{\mathbf{z}}_r) d\phi \cos \theta d\theta} \\ &= v / \xi \end{aligned} \quad (67)$$

where we use the relations $\delta(\mathbf{u} \cdot \hat{\mathbf{z}}_r) = \delta(\hat{\mathbf{u}} \cdot \hat{\mathbf{z}}_r) / |\mathbf{u}|$ and $v = |\mathbf{u}|$ and recognize that the denominator is now simply the arc length ξ of Ω_ξ along the great circle. This arc length depends on the region of frequency space that \mathbf{u} is in (Figures 24 and 25)

$$G(\mathbf{u}) = G_c(\mathbf{u}) = \begin{cases} \frac{v}{2\pi} & |\psi| \leq \Theta \\ \frac{v}{4 \sin^{-1} \left(\frac{\sin \Theta}{|\sin \psi|} \right)} & |\psi| > \Theta \end{cases} \quad (68)$$

which is the Colsher filter of Eq. (56).

Equation (66) is a necessary and sufficient condition that must be met by any valid reconstruction filter. Although these filters will all produce accurate reconstructions with consistent projection data that are noiseless and continuous (Clack, 1992), the behavior of filters will differ in how they propagate inconsistent data introduced by noise or discretization, that is, data that do not fit the model of Eq. (59). There are two classes of filters that satisfy Eq. (66)—factorizable and nonfactorizable.

2. Factorizable Reconstruction Filters

The Colsher filter, Eq. (68), is an example of a *factorizable* filter, which is any FBP filter that can be expressed as the product of a central section through a three-dimensional filter function $G(\mathbf{u})$ and an even positive function $w(\hat{\mathbf{z}}_r)$ that depends only on the direction vector $\hat{\mathbf{z}}_r$, that is:

$$G^1(\mathbf{u}; \hat{\mathbf{z}}_r) = G(\mathbf{u}) w(\hat{\mathbf{z}}_r) \quad (69)$$

with \mathbf{u} constrained to the plane $\mathbf{u} \cdot \hat{\mathbf{z}}_r = 0$. For the Colsher filter $w(\hat{\mathbf{z}}_r) = 1$, whereas for any other valid nonconstant $w(\hat{\mathbf{z}}_r)$ the filter is uniquely determined by Eqs. (66) and (69) (Schorr and Townsend, 1981):

$$G(\mathbf{u}) = \frac{1}{\iint_{\Omega_\Theta} \delta(\mathbf{u} \cdot \hat{\mathbf{z}}_r) w(\hat{\mathbf{z}}_r) d\phi \cos \theta d\theta} \quad (70)$$

as long as $\iint_{\Omega_\Theta} \delta(\mathbf{u} \cdot \hat{\mathbf{z}}_r) w(\hat{\mathbf{z}}_r) d\phi \cos \theta d\theta \neq 0$.

Among the important properties of factorizable FBP filters, such as the Colsher filter, is the ability to commute the order of filtering and backprojection. The FBP filter function on the plane $\mathbf{u} \cdot \hat{\mathbf{z}}_r = 0$ is a two-dimensional section through the origin (at the appropriate angle) of the three-dimensional filter used for BPF, as illustrated in Figure 26. This is similar to the equivalence of the two-dimensional FBP and BPF algorithms (Eqs. (36) and (29)).

An additional property of factorizable filters is the ramp-like behavior due to the relation $\delta(\mathbf{u} \cdot \hat{\mathbf{z}}_r) = \delta(\hat{\mathbf{u}} \cdot \hat{\mathbf{z}}_r) / |\mathbf{u}|$ used in Eq. (67). Finally, we note that factorizable filters, and the Colsher filter in particular, have optimally low noise-propagation properties due to the minimum norm properties of $G_c(\mathbf{u})$ (Defrise *et al.*, 1990).

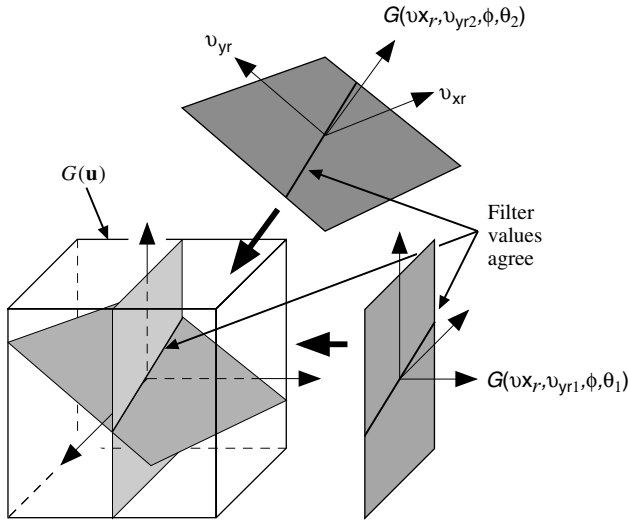


FIGURE 26 Factorizable FBP filter $G(v_{xr}, v_{yr}, \phi, \theta)$ at two different orientations $\hat{z}_r(\phi_1, \theta_1)$ and $\hat{z}_r(\phi_2, \theta_2)$. If $w(\hat{z}_r) = 1$ in Eq. (69), then the two filter sections agree along the line of intersection within a three-dimensional function $G(\mathbf{u})$. This property is not true for nonfactorizable FBP filters.

3. Nonfactorizable Reconstruction Filters

In contrast to the factorizable FBP filters, there is a more general class of FBP filters $G^1(\mathbf{u}; \hat{z}_r)$ for which a factorization of the type in Eq. (69) (Figure 26) is not possible. In other words, using the notation $G(v_{xr}, v_{yr}, \phi, \theta) = G^1(\mathbf{u}; \hat{z}_r)$, $G(v_{xr}, v_{yr}, \phi, \theta)$ is not equivalent to two-dimensional central sections of *any* function $G(\mathbf{u})$, even with a direction-weighting term $w(\hat{z}_r)$.

Although nonfactorizable filters have less favorable noise-propagation properties than factorizable filters (Defrise *et al.*, 1990), they do have the ability to allow for direct reconstruction of truncated projections (Defrise *et al.*, 1995), and two examples of this are the TTR filter (Ra *et al.*, 1992) and the FAVOR filter (Comtat *et al.*, 1993). These filters can be used with truncated X-ray transform data (Figure 7) without resorting first to the computationally intensive forward-projection step of the 3DRP algorithm (Section VA).

An interesting aspect of the relationship between factorizable and nonfactorizable filters is the existence of nontrivial null filters (Clack, 1992). If $G_{NF}^1(\mathbf{u}; \hat{z}_r)$ is a nonfactorizable filter and $G_F^1(\mathbf{u}; \hat{z}_r)$ is a factorizable filter, then the difference

$$N^1(\mathbf{u}; \hat{z}_r) = G_{NF}^1(\mathbf{u}; \hat{z}_r) - G_F^1(\mathbf{u}; \hat{z}_r) \quad (71)$$

is a nonfactorizable filter that has the unusual property

$$\iint_{\Omega_\theta} F_2^{-1} \{ P(v_{xr}, v_{yr}, \phi, \theta) N(v_{xr}, v_{yr}, \phi, \theta) \} d\phi \cos \theta d\theta = 0 \quad (72)$$

for any consistent projection data that satisfy Eq. (6) or (59). Equation (72) can be regarded as a general class of

consistency conditions for (nontruncated) three-dimensional X-ray transform data.

4. General Filter Functions and Properties

If there is an arbitrary function $Q^1(\mathbf{u}; \hat{z}_r)$ such that $T_Q(\mathbf{u})$ exists for Eq. (66) but $T_Q(\mathbf{u}) \neq 1$, it is still possible to use $Q^1(\mathbf{u}; \hat{z}_r)$ as the basis of a filter that satisfies the filter equation, Eq. (66) (Defrise *et al.*, 1993). The most straightforward approach is to use a multiplicative normalization in frequency space:

$$G^1(\mathbf{u}; \hat{z}_r) = Q^1(\mathbf{u}; \hat{z}_r) / T_Q(\mathbf{u}) \quad (73)$$

as long as $T_Q(\mathbf{u}) \neq 0$. An alternative approach that does not require $T_Q(\mathbf{u}) \neq 0$ is to use an additive normalization:

$$G^1(\mathbf{u}; \hat{z}_r) = Q^1(\mathbf{u}; \hat{z}_r) + \frac{w(\hat{z}_r)(1 - T_Q(\mathbf{u}))}{\iint_{\Omega_\theta} \delta(\mathbf{u} \cdot \hat{z}_r) w(\hat{z}_r) d\hat{z}_r} \quad (74)$$

as long as $\iint_{\Omega_\theta} \delta(\mathbf{u} \cdot \hat{z}_r) w(\hat{z}_r) d\hat{z}_r \neq 0$.

It is straightforward to verify that an FBP filter constructed using Eq. (73) or (74) is a solution to the filter equation and will thus correctly reconstruct objects from consistent projection data when used in a three-dimensional FBP algorithm. Such filters can be useful if, for example, the function $Q^1(\mathbf{u}; \hat{z}_r)$ is nearly correct or has useful properties and only a small correction is needed. The approach was used in the derivation of the FAVOR filter, where the function $Q^1(\mathbf{u}; \hat{z}_r)$ corresponded to simple (and fast) one-dimensional ramp-filtering of the projection data (Comtat *et al.*, 1993). Although this approach will work for any function $Q^1(\mathbf{u}; \hat{z}_r)$, large correction terms will necessarily increase the propagation of statistical noise.

E. Other Three-Dimensional Reconstruction Methods

The alternative methods described in Sections IVC1, IVD, and IVE for two-dimensional image reconstruction are also applicable to three-dimensional image reconstruction, albeit with some significant differences and the addition of an entirely new class of methods using rebinning techniques.

1. Inverse Radon Transform

With a set of X-ray transform projection data (Eq. 59), the three-dimensional Radon transform (Eq. 8) can be calculated by summing all the line-integral data (Eq. 59) that lie on the plane defined by t and $\hat{\mathbf{o}}$ (Figure 8) and are parallel to a fixed direction \hat{z}_r that is perpendicular to $\hat{\mathbf{o}}$ (Stazyk *et al.*, 1992):

$$f(t, \hat{\mathbf{o}}) = \int_{-\infty}^{\infty} p(t\hat{\mathbf{o}} + \alpha\hat{z}_r \times \hat{\mathbf{o}}, \hat{z}_r) d\alpha \quad (75)$$

where $\hat{z}_r \times \hat{\mathbf{o}}$ is the vector cross-product. We can improve our estimate of $f(t, \hat{\mathbf{o}})$ by averaging Eq. (75) over all directions

\hat{z}_r with $\hat{z}_r \cdot \hat{\phi} = 0$. This approach has the advantage that the averaged Radon transform incorporates the SNR improvements of the data redundancy of the three-dimensional X-ray transform but does not contain redundant information itself, and thus $f(\mathbf{x})$ can be computed with the inverse three-dimensional Radon transform (Deans, 1983). Effectively, the formation of the averaged Radon transform is a data reduction step because the dimensionality of the data goes from $\mathbb{R}^2 \times \mathbb{S}^2$ to $\mathbb{R}^1 \times \mathbb{S}^2$. The disadvantages of this procedure are similar to a direct Fourier interpolation method because complex interpolations are required. We note that there is a direct relationship between the filter equation and the averaged Radon transform (Defrise *et al.*, 1993).

2. Direct Fourier Methods

As in two-dimensional image reconstruction, it is possible to directly interpolate from the sampling of the Fourier transform supplied by $P_{ijkl} = P(i\Delta v_x, j\Delta v_y, k\Delta\phi, l\Delta\theta)$ to a rectangular volumetric sampling $F_{i'j'k'} = F(i'\Delta v_x, j'\Delta v_y, k'\Delta\phi)$ suitable for inversion with FFTs. Such an approach has similar advantages and disadvantages compared to FBP algorithms as the two-dimensional case. One advantage of a three-dimensional direct Fourier method is that the sampling in the axial direction is similar to the linogram format, thus simplifying the interpolation procedure in the axial direction during the three-dimensional ray tracing of the backprojection process. Three-dimensional direct Fourier methods have been implemented via gridding methods using standard voxel basis functions (Stearns *et al.*, 1990), and with MKB basis functions (Matej and Lewitt, 2001).

3. List-Mode Methods

As mentioned in Section IVD1, three-dimensional list-mode data can be reconstructed by first histogramming the data into projections. This can be followed by any of the three-dimensional reconstruction methods described in this chapter. For imaging systems with few events per scanner LOR, however, this can be a very inefficient mode of data processing and storage and can lead to high levels of statistical noise unless considerable regularization (smoothing) is applied. In these situations three-dimensional iterative methods are often used to reconstruct such list-mode data. Three-dimensional iterative methods also have the advantage of using the same functional form as two-dimensional methods, so they are often simpler to implement than three-dimensional analytic methods, albeit often at the expense of increased computation time.

4. Planogram Methods

The planogram data format is the generalization to three-dimensional imaging of the linogram format (Section IVD2), which is appropriate for flat panel detectors. As in the linogram format, backprojection can be efficiently carried out by

using only FFT operations. The reconstruction of planogram data has been implemented with BPF algorithms, although FBP methods are also under development (Brasse *et al.*, 2000).

5. Cone-Beam Methods

The cone-beam, or divergent three-dimensional X-ray, transform (Natterer, 1986) is not discussed here because the reconstruction procedures are considerably more complex than for the parallel X-ray transform data. There is no equivalent to the central section theorem for divergent projection data. There is, however, a direct relationship between cone-beam data and the derivative of the three-dimensional Radon transform of the object. Thus most cone-beam reconstruction methods are based on either iterative methods or analytic functions related to the three-dimensional Radon transform. There have been numerous recent developments in analytic cone-beam reconstruction methods, particularly in relation to the development of multirow X-ray CT scanners, and the interested reader is referred to the proceedings of the 3D Meetings ("1991 International Meeting," 1992; "1993 International Meeting," 1994; "1995 International Meeting," 1996; "1997 International Meeting," 1998; "1999 International Meeting," 2001; "2001 International Meeting," 2002).

6. Rebinning Methods

With three-dimensional X-ray transform data it is possible to use the measured data to estimate a stacked (volumetric) set of two-dimensional transverse sinograms (Eq. 4) by using some form of signal averaging, similar to the averaged three-dimensional Radon transform described in Section VE1. Such a procedure is called a rebinning algorithm. Rebinning algorithms have the advantage that each rebinned sinogram can be efficiently reconstructed with either analytic or iterative two-dimensional reconstruction methods. In addition, rebinning can significantly reduce the size of the data. The disadvantages of the rebinning methods are that they either pay a penalty in terms of a spatially varying distortion of the PSF or amplification of statistical noise or both. Although rebinning methods are not specifically a reconstruction procedure, they are an important addition to the array of techniques that bear on three-dimensional image reconstruction problems.

The simplest, but still often useful, rebinning method is the single-slice rebinning (SSRB) algorithm (Daube-Witherspoon and Muehlelehner, 1987) in which the rebinned sinograms $p_R(x_r, \phi, z)$ are calculated as

$$P_R(x_r, \phi, z) = \frac{1}{2\theta_{\max}(z)} \int_{-\theta_{\max}(z)}^{\theta_{\max}(z)} p(x_r, y_r = z \cos \theta, \phi, \theta) \cos \theta d\theta \quad (76)$$

where $\theta_{\max}(z)$ is the maximum range of the co-polar angle for LORs crossing the transverse plane at distance z .

The summed LOR data are normalized by the term $1/[2\theta_{\max}(z)]$ to (approximately) compensate for the nonuniform sampling of the rebinned sinograms.

Equation (76) ignores the co-polar angle, so that the LOR is placed in the transverse LOR that bisects the original LOR. This method is accurate for sources near the scanner axis (Kinahan and Karp, 1994), but there is increasing distortion of the PSF for sources further from the scanner axis (Sossi *et al.*, 1994).

A more accurate rebinning method is the Fourier rebinning (FORE) algorithm (Defrise, 1995; Defrise *et al.*, 1997), which is based on a reasonably accurate equivalence between specific elements in the Fourier transformed oblique and transverse sinograms. In other words, the Fourier transformed oblique sinograms can be resorted into transverse sinograms and, after normalization for the sampling of the Fourier transform, inverse transformed to recover $p_R(x_r, \phi, z)$. The FORE method amplifies statistical noise slightly compared to SSRB, but yields a significantly less distorted PSF. The combination of FORE with appropriately weighted two-dimensional iterative reconstruction methods for each rebinned sinogram has successfully been employed for the reconstruction of three-dimensional whole-body PET data in clinically feasible times (Comtat *et al.*, 1998). One disadvantage of FORE relative to SSRB is that because the Fourier transform is computed, FORE cannot be applied to list-mode data, unlike SSRB.

VI. SUMMARY

The goals of this chapter are two. First, we have provided a theoretical basis for the core concepts of two- and three-dimensional analytic image reconstruction from X-ray projections. In particular, with the aid of the central section theorem in its various guises, we have shown how the image reconstruction problem is formed by Fourier transform sampling of the object. The use of the central section theorem also leads to the necessary and sufficient data conditions. Second, we have highlighted the literature that has evolved in the 1990s regarding more esoteric aspects of three-dimensional FBP reconstruction filters, which have a rich complexity not found in two-dimensional image reconstruction, and for which other uses may be found in the future.

References

- 1991 International Meeting on Fully Three-Dimensional Image Reconstruction in Nuclear Medicine and Radiology. (1992). *Phys. Med. Biol.* **37**.
- 1993 International Meeting on Fully Three-Dimensional Image Reconstruction in Radiology Nuclear Medicine. (1994). *Phys. Med. and Biol.* **39**.
- 1995 International Meeting on Fully Three-Dimensional Image Reconstruction in Radiology and Nuclear Medicine. (1996). In "Three-Dimensional Image Reconstruction in Radiology and Nuclear Medicine, Vol. 4, *Computational Imaging and Vision*" (P. Grangeat and J.-L. Amans, eds) Kluwer, Dordrecht, The Netherlands.
- 1997 International Meeting on Fully Three-Dimensional Image Reconstruction in Radiology and Nuclear Medicine. (1998). *Phys. Med. Biol.* **43**.
- 1999 International Meeting on Fully Three-Dimensional Image Reconstruction in Radiology and Nuclear Medicine. (2001). *IEEE Trans. Med. Imag.* **45**.
- 2001 International Meeting on Fully Three-Dimensional Image Reconstruction in Radiology and Nuclear Medicine. (2002). *Phys. Med. Biol.* **47**.
- Bracewell, R. (1965). "The Fourier Transform and Its Applications." McGraw-Hill, New York.
- Brasse, D., Kinahan, P. E., Clackdoyle, R., Comtat, C., Defrise, M., and Townsend, D. W. (2004). Fast fully 3D image reconstruction in PET using planograms. *IEEE Trans. Med. Imag.* **23**: 413–425.
- Clack, R. (1992). Towards a complete description of three-dimensional filtered backprojection. *Phys. Med. Biol.* **37**: 645–660.
- Colsher, J. G. (1980). Fully three-dimensional positron emission tomography. *Phys. Med. Biol.* **25**: 103–115.
- Comtat, C., Kinahan, P. E., Defrise, M., Michel, C., and Townsend, D. W. (1998). Fast reconstruction of 3D PET data with accurate statistical modeling. *IEEE Trans. Nucl. Sci.* **45**: 1083–1089.
- Comtat, C., Morel, C., Defrise, M., and Townsend, D. W. (1993). The FAVOR algorithm for 3D PET data and its implementation using a network of transputers. *Phys. Med. Biol.* **38**: 929–944.
- Crawford, C. R. (1991). CT filtration aliasing artifacts. *IEEE Trans. Med. Imag.* **10**: 99–102.
- Daube-Witherspoon, M. E., and Muehllehner, G. (1987). Treatment of axial data in three-dimensional PET. *J. Nucl. Med.* **28**: 1717–1724.
- Deans, S. R. (1983). "The Radon Transform and Some of Its Applications." John Wiley, New York.
- Defrise, M. (1995). A factorization method for the 3D X-ray transform. *Inverse Probl.* **11**: 983–994.
- Defrise, M., Clack, R., and Townsend, D. (1993). Solution to the three-dimensional image reconstruction problem from two-dimensional projections. *J. Opt. Soc. A* **10**: 869–877.
- Defrise, M., Clack, R., and Townsend, D. W. (1995). Image reconstruction from truncated, two-dimensional parallel projections. *Inverse Probl.* **11**: 287–313.
- Defrise, M., and Kinahan, P. (1998). Data acquisition and image reconstruction for 3D PET. In "The Theory and Practice of 3D PET, Vol. 32, Developments in Nuclear Medicine" (D. W. Townsend and B. Bendriem, eds), pp. 11–54. Kluwer Academic, Dordrecht.
- Defrise, M., Kinahan, P. E., Townsend, D. W., Michel, C., Sibomana, M., and Newport, D. F. (1997). Exact and approximate rebinning algorithms for 3-D PET data. *IEEE Trans. Med. Imag.* **16**: 145–158.
- Defrise, M., Townsend, D. W., and Clack, R. (1989). Three-dimensional image reconstruction from complete projections. *Phys. Med. Biol.* **34**: 573–587.
- Defrise, M., Townsend, D. W., and Deconinck, F. (1990). Statistical noise in three-dimensional positron tomography. *Phys. Med. Biol.* **35**: 131–138.
- Edholm, P. R., and Herman, G. T. (1987). Linograms in image reconstruction from projections. *IEEE Trans. Med. Imag.* **MI-6**: 301–307.
- Edholm, P. R., Herman, G. T., and Roberts, D. A. (1988). Image reconstruction from linograms: Implementation and evaluation. *IEEE Trans. Med. Imag.* **7**: 239–246.
- Herman, G. T. (1980). "Image Reconstruction from Projections." Academic Press, New York.
- Kak, A. C., and Slaney, M. (1988). "Principles of Computerized Tomographic Imaging." IEEE Press, New York.
- Keinert, F. (1989). Inversion of k -plane transforms and applications in computed tomography. *SIAM Rev.* **31**: 273–298.

- Kinahan, P. E., and Karp, J. S. (1994). Figures of merit for comparing reconstruction algorithms with a volume-imaging PET scanner. *Phys. Med. Biol.* **39**: 631–638.
- Kinahan, P. E., and Rogers, J. G. (1989). Analytic 3D image reconstruction using all detected events. *IEEE Trans. Nucl. Sci.* **36**: 964–968.
- Kinahan, P. E., Rogers, J. G., Harrop, R., and Johnson, R. R. (1988). Three-dimensional image reconstruction in object space. *IEEE Trans. Nucl. Sci.* **35**: 635–640.
- Leahy, R., and Qi, J. (2000). Statistical approaches in quantitative positron emission tomography. *Statist. Comp.* **10**: 147–165.
- Lewitt, R. M. (1992). Alternatives to voxels for image representation in iterative reconstruction algorithms. *Phys. Med. Biol.* **37**: 705–716.
- Magnusson, M. (1993). Linogram and other direct methods for tomographic reconstruction. Ph.D. thesis, Linköping University.
- Matej, S., and Lewitt, R. M. (2001). 3D-FRP: Direct Fourier reconstruction with Fourier reprojection for fully 3D PET. *IEEE Trans. Nucl. Sci.* **48**: 1378–1385.
- Natterer, F. (1986). “The Mathematics of Computerized Tomography.” John Wiley, New York.
- Natterer, F., and Wübbeling, F. (2001). “Mathematical Methods in Image Reconstruction.” SIAM, Philadelphia.
- Ollinger, J. M., and Fessler, J. A. (1997). Positron emission tomography. *IEEE Sig. Processing Mag.* **14**: 43–55.
- Orlov, S. S. (1976a). Theory of three-dimensional image reconstruction I. Conditions for a complete set of projections. *Sov. Phys. Crystallog.* **20**: 429–433.
- Orlov, S. S. (1976b). Theory of three-dimensional image reconstruction II. The recovery operator. *Sov. Phys. Crystallog.* **20**: 429–433.
- O’Sullivan, J. D. (1985). A fast sinc function gridding algorithm for Fourier inversion in computer tomography. *IEEE Trans. Med. Imag.* **MI-4**: 200–207.
- Ra, J. B., Lim, C. B., Cho, Z. H., Hilal, S. K., and Correll, J. (1992). A true 3D reconstruction algorithm for the spherical positron tomograph. *Phys. Med. Biol.* **27**: 37–50.
- Schorr, B., and Townsend, D. (1981). Filters for three-dimensional limited-angle tomography. *Phys. Med. Biol.* **26**: 305–312.
- Shung, K. K., Smith, M. B., and Tsui, B. M. W. (1992). “Principles of Medical Imaging.” Academic Press, San Diego.
- Sossi, V., Stazyk, M., Kinahan, P. E., and Ruth, T. (1994). The performance of the single-slice rebinning technique for imaging the human striatum as evaluated by phantom studies. *Phys. Med. Biol.* **39**: 369–375.
- Stazyk, M., Rogers, J., and Harrop, R. (1992). Analytic image reconstruction in PVI using the 3D Radon transform. *Phys. Med. Biol.* **37**: 689–704.
- Stearns, C. W., Chesler, D. A., and Brownell, G. L. (1990). Accelerated image reconstruction for a cylindrical positron tomograph using Fourier domain methods. *IEEE Trans. Nucl. Sci.* **37**: 773–777.
- Stearns, C. W., Crawford, C. R., and Hu, H. (1994). Oversampled filters for quantitative volumetric PET reconstruction. *Phys. Med. Biol.* **39**: 381–388.
- Barrett, H. H., and Swindell, W. (1981). “Radiological Imaging.” Academic Press, New York.